ISSN 2072-5981
doi: 10.26907/mrsej

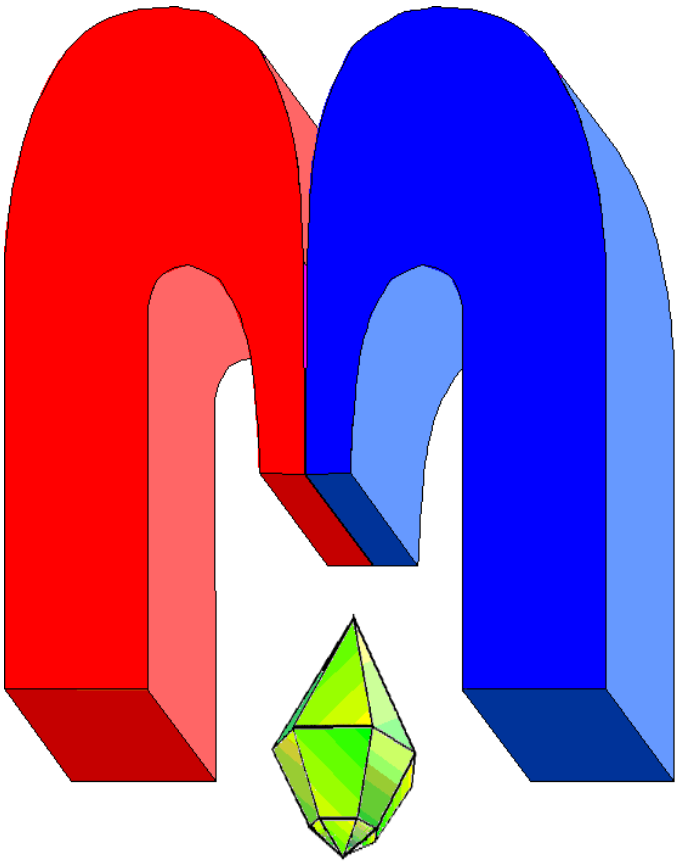

Magnetic Resonance in Solids

Electronic Journal

Volume ***23***
Issue ***1***
Article No ***21101***
1-29 pages
2021
doi: **10.26907/mrsej-21101**

http://mrsej.kpfu.ru
http://mrsej.ksu.ru

Established and published by Kazan University
Endorsed by International Society of Magnetic Resonance (ISMAR)
Registered by Russian Federation Committee on Press (#015140),
August 2, 1996
First Issue appeared on July 25, 1997

"***Magnetic Resonance in Solids. Electronic Journal***" (**MRS*ej***) is a peer-reviewed, all electronic journal, publishing articles which meet the highest standards of scientific quality in the field of basic research of a magnetic resonance in solids and related phenomena.

Indexed and abstracted by
Web of Science (*ESCI*, Clarivate Analytics, from 2015), *Scopus* (Elsevier, from 2012), *RusIndexSC* (*eLibrary*, from 2006), *Google Scholar*, *DOAJ*, *ROAD*, *CyberLeninka* (from 2006), *SCImago Journal & Country Rank*, etc.

* In Kazan University the Electron Paramagnetic Resonance (EPR) was discovered by Zavoisky E.K. in 1944.

Simulation of four-, five-, and six-pulse Double Quantum Coherence signals for nitroxide biradicals: Distance measurement in biological systems

S.K. Misra*, H.R. Salahi

Physics Department, Concordia University, 1455 de Maisonneuve Boulevard West, Montreal, Quebec H3G 1M8, Canada

* *E-mail: sushil.misra@concordia.ca*

‡ *E-mail: hamidreza.salahi@concordia.ca*

(Received April 30, 2021; revised June 2, 2021; accepted June 7, 2021; published June 15, 2021)

Algorithms are developed to calculate pulsed EPR (Electron Paramagnetic Resonance) signals, utilized for distance measurements in biological systems, using nitroxide biradicals, for the cases of: (i) four- (ii) five- and (iii) six-pulse double quantum coherence (DQC). The details of how to calculate the signals analytically and numerically are provided. It is shown that only one-dimensional experiments are needed to determine the dipolar constant, from which the distance between the two nitroxides of the biradical can be extracted directly. The analytical expressions reveal that for the case of non-selective pulses the Fourier transforms of these three DQC pulse sequences exhibit two predominant peaks at $\pm d \times \left(3\cos^2\theta - 1\right)$; where $d = \frac{2}{3}D$, with D being the dipolar-coupling constant and θ being the orientation of the dipolar axis with respect to the external magnetic field. It is shown here that the DQC signal is broadened by relaxation only for the four-pulse sequence, but not for the five- and six-pulse sequences. The rigorous numerical algorithm developed here is shown to produce very good agreement of the simulated signals with the published experimental signals for four-, five-, and six- pulse DQC sequences. It is discussed that the two-dimensional Fourier transform of the six-pulse signal, calculated in terms of the dipolar and echo times, gives information about the dipolar constant when analyzed along the dipolar axis, whereas its variation along the echo-axis provides information on the frequency-swept ESR spectrum of the two nitroxides.

PACS: 76.30.-v, 76.70.Dx

Keywords: pulsed EPR, double quantum coherence, Liouville-von Neumann equation, stretched exponential, relaxation

1. Introduction

Pulsed electron paramagnetic resonance (EPR) has been exploited as a powerful technique to unravel the electronic and geometric structures around paramagnetic centers in detail. It has been widely exploited in biology, chemistry, physics, and materials science. Weak interactions between electron spins, as well as those between electron and nuclear spins, not resolved by continuous wave (CW) EPR, can be distinguished by pulsed EPR. To analyze pulsed EPR spectra, a rigorous simulation is necessary to extract information on properties of the system, such as orientational selectivity [1], dipolar-interaction constant between the two nitroxide magnetic dipoles, which in, turn, enables determination of the distance between the nitroxides from the pulsed EPR data correctly. Multi-pulse EPR has been exploited for distance measurements in biological systems [1–13]. A full treatment of the problem will here be carried out for the calculation of Pake doublets in polycrystalline averages for the four-, five, and six-pulse DQC (Double Quantum Coherence) signals, which are direct measures of the dipolar interaction, from which the distance between the two nitroxide dipoles in the nitroxide biradical, used as spin probe, can be determined, by using the expression that relates the distance in Å to the dipolar constant d, expressed in MHz: $r[\text{Å}] = (10\,\text{Å})[(52.04\,\text{MHz})/d]^{1/3}$, where $d = \frac{2}{3}D$, with D being the dipolar-

coupling constant. To this end, it is useful to have analytical expressions to deduce the peaks in the time-dependent and Fourier transforms of the pulsed EPR signals. On the other hand, it is easier and more rigorous to calculate numerically the pulsed EPR signal, since the analytical expressions, which are derived with some approximations, become lengthier and unwieldy to manipulate as the number of pulses increases.

In particular, experimental results have been reported on the double quantum coherence signals involving four-, five-, and six-pulse sequences [3]. However, no attempts have been made to calculate them either using analytical expression, or by rigorous numerical simulation. To this end, it is useful to have analytical expressions for pulsed EPR signals to deduce the peaks in the time-dependent and Fourier transforms of the pulsed EPR signals. On the other hand, it is easier and more rigorous to calculate numerically the pulsed EPR signal, since the analytical expressions become lengthier and unwieldy to manipulate as the number of pulses increases.

It is the purpose of this paper to derive (i) analytical expressions using Mathematica for four-, five- and six-pulse double quantum coherence (DQC) EPR signals for an arbitrary orientation of the external magnetic field with respect to the dipolar axis, and (ii) to simulate numerically, using Matlab, the powder averages using full numerical diagonalizations of the pulse- and/or spin-Hamiltonian matrices, exploiting the algorithm of Misra, Borbat and Freed [2] to calculate the various multi-pulse DQC signals. The simulations are carried out here for a fixed value of r, which can be exploited if required when the probabilities for distance distribution are considered. The developed analytical expressions, as well as the numerical algorithm developed here, will be applied to analyze the data reported and discussed by Borbat and Freed [3] on the double quantum coherence signals involving four-, five-, and six-pulse sequences . In order to compare the efficiencies of the four-, five- and six-pulse DQC sequences, the depths of their dipolar modulations will here be calculated and compared with those achieved, by other techniques, e.g., DEER (Double Electron-Electron Resonance) and RIDME (Relaxation Induced Dipolar Modulation Enhancement).

The organization of this paper is as follows. Section 2 deals with the required theoretical background, including the spin- and pulse-Hamiltonians, for the nitroxide biradical, along with the flow-chart for calculation of the signal. Derivation of full analytical expressions for four-, five-, and six- pulse sequences are given in detail in Sec. 3. The numerical algorithm to simulate the pulsed-EPR signals in the absence of relaxation for a polycrystalline sample is provided in Sec 4. The effect of spin relaxation for a given orientation of the dipolar axis with respect to the external magnetic field and the orientations of the magnetic dipoles of the two nitroxides of the biradical is considered in Sec. 5, including the spin relaxation in a polycrystalline sample, using the stretched-exponential approach [14, 15]. The relative merits of the four-, five- and six-pulse DQC sequences for distance measurement are discussed in Sec 6. The modulation depths for the three sequences will be calculated in Sec. 7. In Sec. 8, numerical results of simulations to fit published experimental data [3] for the four-, five-, and six-pulse sequences are presented. The conclusions are summarized in Sec. 9.

2. Theoretical Details

In this section, the theory, and the procedure to calculate the two-dimensional (2D) EPR signal for a coupled nitroxides biradical are described, along with their reduction to one-time signal at the top of echo. The biradical system considered consists of two nitroxides, each characterized by an electron with spin $S = 1/2$ and a nucleus with spin $I = 1$. The calculations will here be carried out in the Hilbert space of dimension 36×36.

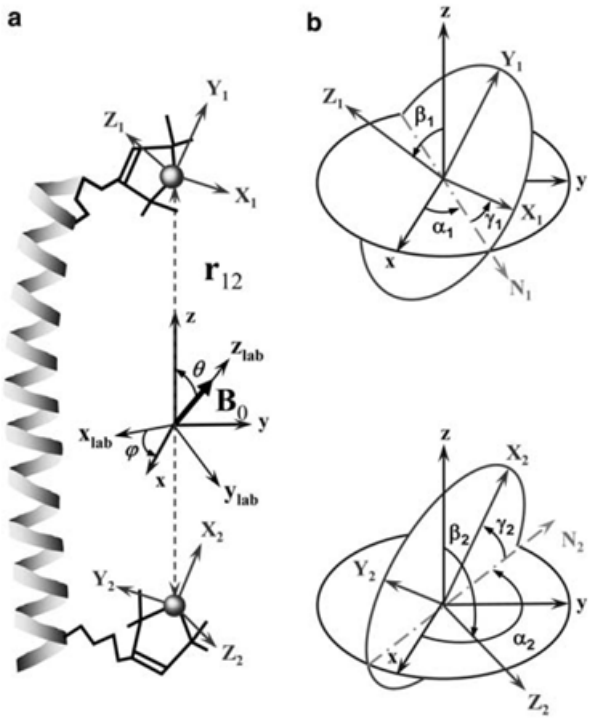

Figure 1. (a) The two nitroxides in the biradical in the dipolar frame of reference. The z-axis of the dipolar frame is chosen to be along the vector $\mathbf{r}_{12}$ connecting the magnetic dipoles of the nitroxides. The relative orientation of the laboratory-fixed frame (with its $z_{\mathtt{lab}}$ axis along the external magnetic field B_0) and the dipolar frame is defined by the Euler angles $\eta = (0, \theta, \phi)$ (b) The set of Euler angles $\lambda_k = (\alpha_k, \beta_k, \gamma_k), (k = 1, 2)$, which define the orientations of the hyperfine and g-matrix principal axes for nitroxides 1 and 2 in the dipolar frame with respect to molecular frame of reference (denoted by $X_k, Y_k, Z_k, k = 1, 2$); here N_1 and N_2 are the lines of nodes for the two nitroxide frames. For the numerical calculations in the present work, the x axis of the first nitroxide magnetic frame is chosen to be along the line of nodes of the first nitroxide, N_1, so the value of α_1 becomes zero. (This figure is reproduced from [8] by permission.)

2.1. Static Spin Hamiltonian

The spin Hamiltonian for the coupled nitroxides system of the biradical is expressed in the rotating frame as [1]:

$$H_0 = H_{01} + H_{02} + H_{12} = \sum_{k=1,2} \{C_k S_{z_k} + A_k S_{z_k} I_{z_k} + B_k S_{z_k} I_{+_k} + B_k^* \, S_{z_k} I_{-_k}\}$$
$$+ \left\{ \frac{D}{2} \left(3\cos^2\theta - 1\right) \left(S_z^2 - \mathbf{S^2}/3\right) + J \left(\frac{1}{2} - 2\mathbf{S_1}.\mathbf{S_2}\right) \right\}. \quad (1)$$

Here, the first curly bracket represents the static Hamiltonian of the two nitroxide radicals, which includes the Zeeman and hyperfine interactions. The expressions for the coefficients C, A and B as obtained by two successive transformations from the magnetic frames of the nitroxide dipoles to the dipolar axis (Fig. 1), followed by a transformation to the laboratory frame (with its z axis parallel to the external magnetic field); they are provided in Appendix A below; S_{z_k}, I_{z_k},I_{+_k} and I_{-_k} are the spin operators for the two nitroxides. In the second bracket in Eq. (1),

$$D = \frac{3\gamma_e^2 \hbar}{2r^3}. \quad (2)$$

In Eq. (2), γ_e is the gyromagnetic ratio of the electron and $\hbar = h/2\pi$ is the reduced Planck's constant. In the present work, the constant $d = 2/3D$ is used; it will be referred to as the "dipolar constant" hereafter. In Eq. (1), $\mathbf{S}$ represents the total electronic spin for the two nitroxides, expressed in the direct-product space as:

$$\mathbf{S} = \mathbf{S_1} + \mathbf{S_2} = \frac{1}{2}\sigma_1 \otimes \mathbb{I}_{S_2} \otimes \mathbb{I}_{I_1} \otimes \mathbb{I}_{I_2} + \mathbb{I}_{S_1} \otimes \frac{1}{2}\sigma_2 \otimes \mathbb{I}_{I_1} \otimes \mathbb{I}_{I_2}, \tag{3}$$

where $\sigma_k; k = 1, 2$ are expressed in terms of the Pauli spin matrices, $\mathbb{I}_{S_k}$ and $\mathbb{I}_{I_k}; k = 1, 2$ are identity matrices in the electronic 2×2 and nuclear 3×3 spaces, respectively, of the two nitroxide, and $\otimes$ stands for the direct product. The eigenvalues of the Spin Hamiltonian in Eq. (1) is given in Appendix B

2.2. Pulse Hamiltonian

The Hamiltonian of a pulse, with amplitude, B_1, of radiation microwave magnetic field, is given as [1, 2]

$$H_p = \frac{\gamma_e B_1}{2}\left(e^{-i\phi}S_+ + e^{i\phi}S_-\right), \tag{4}$$

where ϕ is the phase of the pulse and $S_\pm$ are the raising/lowering operators of the total electronic spin of the coupled nitroxide system in the 36×36 Hilbert space, which are expressed in the electron-nuclear direct-product space as

$$S_\pm = S_{\pm_{S_1}} \otimes \mathbb{I}_{S_2} \otimes \mathbb{I}_{I_1} \otimes \mathbb{I}_{I_2} + \mathbb{I}_{S_1} \otimes S_{\pm_{S_2}} \otimes \mathbb{I}_{I_1} \otimes \mathbb{I}_{I_2}. \tag{5}$$

2.3. Calculation of multi-pulse EPR signal

The general procedure for calculation of the signal is briefly described as follows. The initial density matrix for the nitroxide biradical is subjected to a pulse, then phase-cycled to follow a chosen coherence pathway over which it evolves freely undergoing relaxation. This is repeated depending on the number of pulses before the final signal is obtained. The flow chart for the calculation of the signal is given in Appendix A, which can be used to derive analytical expression, using some approximation, or for rigorous numerical calculation of the signal. The details of the various steps are described as follows.

2.3.1. Transformation of density matrix by a pulse

During the application of a pulse, the spin relaxation will here be neglected. In that case, the evolution of the density matrix is described in Hilbert space, as follows:

$$\frac{d}{dt}\rho(t) = -i\left[(H_0 + H_p), \rho(t)\right], \tag{6}$$

with H_p being expressed by Eq. (4). The density matrix, as transformed by the application of a pulse of duration t_p. The solution of Eq. (6), neglecting relaxation during the pulse, is given as [1, 2]:

$$\rho(t_0 + t_p) = e^{-i(H_0+H_p)t_p}\rho(t_0)\ e^{i(H_0+H_p)t_p} = P\ \rho(t_0)\ P^\dagger. \tag{7}$$

In Eq. (7), † denotes the Hermitian adjoint of a matrix. The matrix for the propagation operator $P = e^{-i(H_0+H_p)t_p}$ in Eq. (7), has the general form in the electronic magnetic basis [1]:

$$P = \begin{pmatrix} [[P_{11}]] & [[P_{12}]]\ e^{-i\phi} & [[P_{13}]]e^{-i\phi} & [[P_{14}]]e^{-2i\phi} \\ [[P_{21}]]\, e^{i\phi} & [[P_{22}]] & [[P_{23}]] & [[P_{24}]]e^{-i\phi} \\ [[P_{31}]]e^{i\phi} & [[P_{32}]] & [[P_{33}]] & [[P_{34}]]e^{-i\phi} \\ [[P_{41}]]\, e^{2i\phi} & [[P_{42}]]\, e^{i\phi} & [[P_{43}]]\, e^{i\phi} & [[P_{44}]] \end{pmatrix}. \tag{8}$$

In Eq. (8), $[[P_{ij}]]$ are 9×9 matrices in the hyperfine space, with ϕ being the pulse phase Eq. (4). The 9×9 matrix elements of $[[P_{ij}]]$ in the hyperfine space of the propagator operator in Eq. (8) are rather long expressions, but they can be easily can be calculated using *Mathematica*. On the other hand, all significant interpretations of relevance here can be made without including them here. *The double square brackets around* $[[P_{ij}]]$ *will hereafter be dropped, with the understanding that they are* 9×9 *matrices in the hyperfine space.*

2.3.2. Selection of coherence pathways

In the procedure to calculate the signal, the density matrix is projected onto the coherence pathways of interest, after the application of a pulse, which are $p = 0, \pm 1, \pm 2$ as given in Fig. 2 for different pulse sequences. To this end, a projection operator matrix is used that retains only the relevant elements of the density matrix corresponding to the particular pathway, p, putting all the other elements equal to zero. These projection operator matrices for the various coherence pathways, p, are listed in Appendix C.

2.3.3. Free evolution and effect of relaxation on density matrix

The pulsed EPR signal for the system of coupled nitroxides in the absence of a pulse, during free evolution and relaxation is calculated by the use of Liouville von-Neumann (LVN) equation for the time evolution of the reduced density matrix, $\chi = \rho - \rho_0$, with ρ_0 being the initial density matrix, expressed in Eq. (15) in Sec. 3 below, is given by [1, 2]

$$\frac{d}{dt}\chi(t) = -i\left[H_0, \chi(t)\right] + \hat{\hat{\Gamma}}\chi(t), \tag{9}$$

where H_0 is given by Eq. (1). The matrix elements of $\hat{\hat{\Gamma}}$, the relaxation superoperator in Liouville space, in Eq. (9), are:

$$\hat{\hat{\Gamma}}_{ij,kl} = -\delta_{ij}\delta_{kl}\frac{1}{(T_1)_{ik}} - \delta_{ik}\delta_{jl}\left(1 - \delta_{ij}\right)\frac{1}{T_2^{S,D}}. \tag{10}$$

In Eq. (10), $(T_1)_{ik}$ are the spin-lattice relaxation times between the populations ii to kk, operative only on the coherence pathway $p = 0$, and $T_2^{S,D}$ are the spin-spin relaxation times, operative along the $p = \pm 1$, and $p = \pm 2$ pathways, respectively, as shown in Fig. 2. In general, different transitions will have different spin-spin relaxation times, $\left(T_2^{S,D}\right)_{ij}$. However, these relaxation times are only slightly different from each other [16–18], approximated hereafter by an average spin-spin relaxation time $T_2^{S,D}$, e.g., in Eq. (11) below.

The pathway $p = 0$ is not used in the five- and six- pulse DQC sequences (Fig.2). Since the populations appear only on the $p = 0$ pathway, then in Eq. (10), the relaxation times $(T_1)_{ik}$, affecting the populations, have no effect on the signal. Regarding the coherence pathways $p = \pm 1$ and $p = \pm 2$, participating in the five- and six- pulse sequences, only the second term on the right-hand side of Eq. (10) which corresponds to $i \neq j$ elements of the reduced density matrix,

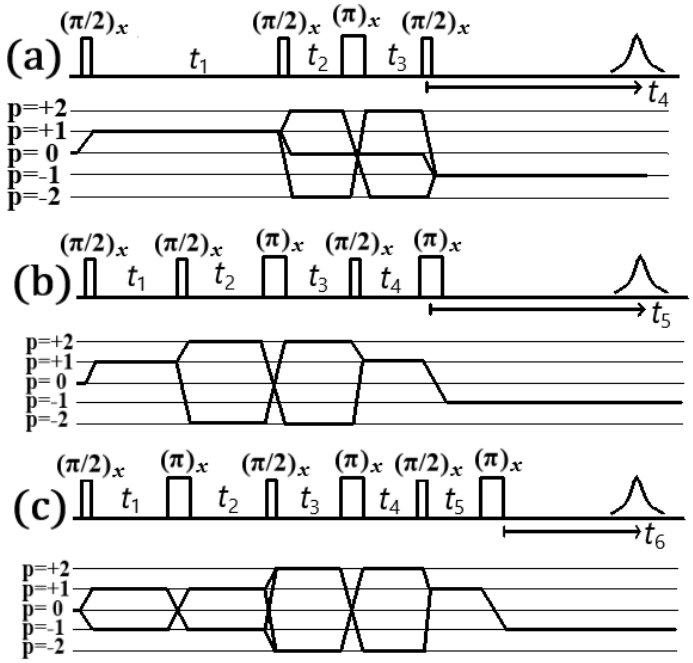

Figure 2. The pulse schemes and the relevant coherence pathways for (a) four-pulse DQC, (b) five-pulse DQC, and (c) six-pulse DQC. Perfect $(\pi/2)_x$ or $(\pi)_x$ pulses are used for all sequences, where the duration of the pulses, t_p, is determined by $t_p = \gamma_e B_1/\beta$, knowing B_1, where B_1 is the amplitude of the microwave field and $\beta = \pi/2$; π is the tip angle; p is the coherence order, which represents transverse magnetization, corresponding to spins rotating in a plane perpendicular to the external field. This figure is reproduced from [3].

produces the effect of relaxation on the final signal. The solution of Eq. (9) after time t, expressing the change in χ_{ij} due to relaxation along the $p = \pm 1, \pm 2$ pathways, is then

$$\chi(t_0 + t) = e^{-t/T_2^{S(D)}} e^{-iH_0 t} \chi(t_0)\ e^{iH_0 t}. \tag{11}$$

The matrix for $e^{-iH_0 t}$ used in Eq. (11) for the coupled nitroxides system is given in Appendix B below.

One also needs to consider the relaxation between the populations for the four-pulse DQC signal, since it includes the coherence pathway $p = 0$ (Fig. 2). This is accomplished by first diagonalizing the non-diagonal part of the relaxation matrix in 36 $\times$ 36 Liouville space, as given by Eq. (10). In the five-pulse experiment, using lower temperatures, the values of the off-diagonal elements of the relaxation matrix $(T_1)_{ik}$ in Eq. (10) for $i \neq k$, are larger than both the spin-spin relaxation times and the duration of the experiment by two order of magnitudes [16]; they are neglected since they do not have any significant effect on the final signal. Thus, only the diagonal elements of the relaxation matrix are retained. The time evolution of the reduced density matrix on the coherence pathway $p = 0$, assuming that they are all equal to each other, is

$$\chi(t_0 + t) = e^{-t/T_1} e^{-iH_0 t} \chi(t_0)\ e^{iH_0 t}. \tag{12}$$

2.3.4. Pulsed EPR Signal

For the calculation of four- five- six-pulse DQC signals, the final density matrix $\rho_f(t_1, ..., t_n)$, with $n = 4, 5, 6$, respectively, with t_k being the time between the kth and $(k+1)$th pulse is obtained by successive applications of the n pulses to the initial density matrix, using Eq. (7)

followed by the application of the relevant coherence pathway projection operator matrix and then the free evolutions over the coherence pathways as shown in Fig. 2, using Eqs. (11) and (12) for coherence pathways $p = \pm 1$, $p = \pm 2$ and $p = 0$, respectively.

For the orientation (θ, ϕ) of the laboratory frame (with its z axis, denoted by $z_{\mathtt{lab}}$, along the static magnetic field as shown in Fig. 1(a)) with respect to the dipolar axis, and the relative orientation of the biradicals, characterized by five independent Euler angles, $(\alpha_1 = 0, \beta_1, \gamma_1, \alpha_2, \beta_2, \gamma_2)$ as shown in Fig 1(b), the complex signal is then calculated as follows:

$$S\left(\{\mathbf{t_k}\}, \theta, \phi, \beta_1, \gamma_1, \alpha_2, \beta_2, \gamma_2\right) = \mathrm{Tr}\left(S_+ \rho_f\right), \tag{13}$$

where $\{\mathbf{t_k}\} = \mathbf{t_1}, \mathbf{t_2}, \ldots, \mathbf{t}_n$ for the calculation of the signal consisting of $n(= 4, 5, 6)$ pulses.

2.3.5. Gaussian inhomogeneous broadening

In order to take into account the Gaussian inhomogeneous broadening effect due to dephasing of spins in the x, y plane after the application of a $\pi/2$ pulse, the final signals

$$S\left(\{\mathbf{t_k}\}, \theta, \phi, \beta_1, \gamma_1, \alpha_2, \beta_2, \gamma_2\right).$$

in Eq. (13) for each orientation (θ, ϕ) are multiplied by the by the same factors $e^{-2\pi^2 \Delta_G^2 (t_4 - t_1)^2}$ for four-pulse DQC, $e^{-2\pi^2 \Delta_G^2 (t_5 - t_{max})^2}$ for five-pulse DQC and $e^{-2\pi^2 \Delta_G^2 (t_6 - t_5)^2}$ for six-pulse DQC, where Δ_G is the Gaussian inhomogeneous broadening parameter. Although, the two nitroxides, in general, experience different dephasing of their respective spins after the application of a $\pi/2$ pulse, since they are not strongly coupled to each other by the exchange interaction, which is assumed to be zero here, their Gaussian inhomogeneous broadening factors are assumed to be the same, on the average, in the present calculations.

3. Analytical expressions for multi-pulse-EPR Signals

In this section, multi-pulse two-dimensional DQC signals will be calculated for hard pulses analytically using the procedure outlined in Sec. 2 above. Here the basis vectors in the magnetic basis, characterized by $|M_{s_1}, M_{s_2}, m_{I_1}, m_{I_2}\rangle$ are used, where $M_{s_1}, M_{s_2}, m_{I_1}, m_{I_2}$ are the two electronic and the two nuclear magnetic quantum numbers, respectively, for the two nitroxides.

3.1. General algorithm to derive analytical expressions for multi-pulse-EPR Signals

For the calculation of multi-pulse sequence signal considered here, one starts with the initial density matrix, ρ_0, in thermal equilibrium. It is governed by the Boltzmann distribution of pupulations for the two electrons, each with spin 1/2. Assuming the high-temperature approximation and neglecting the hyperfine splitting, which is much less than the electronic Zeeman splitting in Ku band with $B_0 = 6200$ G (high field limit), which corresponds to ≈ 17.3 GHz frequency (as listed in Table 2), one has:

$$\rho_0 = \frac{\exp(-\hat{H}_0/kT)}{\mathrm{Tr}\left[\exp(-\hat{H}_0/kT)\right]} \propto \left(\mathbb{1} - \frac{\hbar\,\omega_0}{k_B T} S_Z + \ldots\right). \tag{14}$$

The term $\mathbb{1}$ in Eq. (14) does not contribute to the signal, since $Tr(S_+\,\mathbb{1}\,) = 0$, according to (13), For calculating the signal, ρ_0 , then can be replaced, as follows:

$$\begin{aligned} \rho_0 \;\rightarrow S_Z \; &= S_{z_1} + S_{z_2} = \rho_0 = \left(\frac{\sigma_{z_1}}{2}\right) \otimes \; \mathbb{1}_{S_2} \otimes \mathbb{1}_{I_1} \otimes \mathbb{1}_{I_2} + \mathbb{1}_{S_1} \otimes \left(\frac{\sigma_{z_2}}{2}\right) \otimes \mathbb{1}_{I_1} \otimes \mathbb{1}_{I_2} \\ &= \mathrm{diag}\{[[1]], [[0]], [[0]], [[-1]]\}, \end{aligned} \tag{15}$$

where $\sigma_{z_i}; i = 1, 2$ are the z-components of Pauli spin matrices for the two electrons. The double square bracket in Eq. (15) indicates 9×9 diagonal matrix with its elements equal to that represented in the square bracket. The density matrix, ρ, after the application of the first pulse, is obtained by using Eq. (7). The density matrix on the relevant coherence pathway subsequent to the action of a pulse is obtained by applying the projection operator matrix, P_k, (Appendix B), on the resulting density matrix, ρ. This is accomplished by the product $\rho^{(k)} = P_k \circ \rho$, where $P_k \; ; \; k = 0, \; \pm 1, \; \pm 2$ is the projection operator matrix for the coherence pathway $p = k$ and $\circ$ denotes the Hadamard product of the two matrices, wherein each element i, j of the resulting density matrix is the product of the i, j of the projection operator matrix and the element i, j of the density matrix, ρ.,the density matrix, after free evolution over time t on a coherence pathway, in the absence of relaxation, is calculated by using Eqs. (11), (12) and (B.11) as follows:

For $p = 0$

$$e^{-iH_0 t}\rho^{(0)}e^{iH_0 t} = \begin{pmatrix} \rho_{11} & 0 & 0 & 0 \\ 0 & a_1 & a_2 & 0 \\ 0 & a_3 & a_4 & 0 \\ 0 & 0 & 0 & \rho_{44} \end{pmatrix}, \tag{16}$$

where

$$\begin{aligned} a_1 &\equiv S_1^{(0)}(t)\,\rho_{33} + S_2^{(0)}(t)\,\rho_{23} + S_2^{(0)}(t)^*\,\rho_{32} + S_3^{(0)}(t)\,\rho_{22}, \\ a_2 &\equiv S_1^{(0)}(t)\,\rho_{32} + S_2^{(0)}(t)\,(\rho_{22} - \rho_{33}) + S_4^{(0)}(t)\,\rho_{23}, \\ a_3 &\equiv S_1^{(0)}(t)\,\rho_{23} - S_2^{(0)}(t)^*\rho_{33} + S_2^{(0)}(t)^*\,\rho_{22} + S_4^{(0)}(t)^*\,\rho_{32}, \\ a_4 &\equiv S_1^{(0)}(t)\,\rho_{22} + S_2^{(0)}(t)\,\rho_{23} - S_2^{(0)}(t)^*\,\rho_{32} + S_3^{(0)}(t)\,\rho_{33}. \end{aligned} \tag{17}$$

For $p = +1$

$$e^{-iH_0 t}\rho^{(+1)}e^{iH_0 t} = \begin{pmatrix} 0 & S_1^{(+1)}(t)\,\rho_{12} + S_2^{(+1)}(t)\,\rho_{13} & S_2^{(+1)}(t)\,\rho_{12} + S_5^{(+1)}(t)\,\rho_{13} & 0 \\ 0 & 0 & 0 & S_3^{(+1)}(t)\,\rho_{24} + S_4^{(+1)}(t)\,\rho_{34} \\ 0 & 0 & 0 & S_4^{(+1)}(t)\,\rho_{24} + S_6^{(+1)}(t)\,\rho_{34} \\ 0 & 0 & 0 & 0 \end{pmatrix}. \tag{18}$$

For $p = +2$

$$e^{-iH_0 t}\rho^{(+2)}e^{iH_0 t} = \begin{pmatrix} 0 & 0 & 0 & S_1^{(+2)}(t)\,\rho_{14} \\ 0 & 0 & 0 & 0 \\ 0 & 0 & 0 & 0 \\ 0 & 0 & 0 & 0 \end{pmatrix}, \tag{19}$$

where $\rho^{(0)}$, $\rho^{(+1)}$ and $\rho^{(2)}$ are the density matrices before the free evolutions on pathways $p = 0, \; +1, +2$, respectively, after phase cycling. The $S^{(k)}{}_i\,(t)\,; k = 0, 1, 2$ terms for different coherence pathways, used in Eqs. (16)-(19), are listed in Table 1. The evolutions of the density matrix over the coherence pathways $p = -1$ and $p = -2$ are conjugate transpose of those for $p = +1$ and $p = +2$, respectively, as given above. The resulting density matrix at the end of a coherence pathway will serve as the starting density matrix for the next pulse. The same procedure is repeated for all other pulses in turn to calculate the final density matrix. In the end, the signal for a chosen orientations of the two nitroxide dipoles with respect to the dipolar axis, oriented at an angle θ with respect to the lab axis, is obtained using Eq. (13).

Table 1. The free evolution terms for $p = 0, p = +1$ and $p = +2$ used in the analytical expressions. The superscripts on $S_i(t)$ indicates the coherence pathway. The free evolution terms corresponding to $p = -1$ and $p = -2$ are the adjoint of those for $p = +1$ and $p = +2$, respectively. The components of the vector $\boldsymbol{\Xi}$ are $\Xi_k; k = 1, 2, \ldots, 6$. $S_i^{(j)}(t); i = 1, ..., 6; j = 0, 1, 2$ are 9×9 matrices wherein $\sin(p\,\boldsymbol{\Xi}), p = 1, 2, 4$ and $\cos(\boldsymbol{\Xi})$ are 9×9 diagonal matrices with the diagonal elements being the i-th diagonal element of the matrix of the argument of sin or cos, e.g., $\sin(2\boldsymbol{\Xi}) = [[\sin(2\Xi_i)]]$; the elements $\sin(\Xi_i)$ and $\cos(\Xi_i)$ are defined in Appendix B.

$S_1^{(0)}(t)$	$-\frac{1}{4}\sin^2(2\boldsymbol{\Xi})(e^{it\omega_{23}} + e^{it\omega_{32}} - 2)$
$S_2^{(0)}(t)$	$(-\frac{1}{4}\sin(4\boldsymbol{\Xi}) + \sin(\boldsymbol{\Xi})\cos^3(\boldsymbol{\Xi})e^{it\omega_{23}} - \sin^3(\boldsymbol{\Xi})\cos(\boldsymbol{\Xi})e^{it\omega_{32}})$
$S_3^{(0)}(t)$	$\frac{1}{4}(\cos(4\boldsymbol{\Xi}) + \sin^2(2\boldsymbol{\Xi})(e^{it\omega_{23}} + e^{it\omega_{32}}) + 3)$
$S_4^{(0)}(t)$	$2\sin^2(\boldsymbol{\Xi})\cos^2(\boldsymbol{\Xi}) + \sin^4(\boldsymbol{\Xi})e^{it\omega_{32}} + \cos^4(\boldsymbol{\Xi})e^{it\omega_{23}}$
$S_1^{(+1)}(t)$	$e^{-it\omega_{13}}\sin^2(\boldsymbol{\Xi}) + e^{-it\omega_{12}}\cos^2(\boldsymbol{\Xi})$
$S_2^{(+1)}(t)$	$(e^{-it\omega_{13}} - e^{-it\omega_{12}})\sin(\boldsymbol{\Xi})\cos(\boldsymbol{\Xi})$
$S_3^{(+1)}(t)$	$e^{-it\omega_{34}}\sin^2(\boldsymbol{\Xi}) + e^{-it\omega_{24}}\cos^2(\boldsymbol{\Xi})$
$S_4^{(+1)}(t)$	$(e^{-it\omega_{34}} - e^{-it\omega_{24}})\sin(\boldsymbol{\Xi})\cos(\boldsymbol{\Xi})$
$S_5^{(+1)}(t)$	$e^{-it\omega_{12}}\sin^2(\boldsymbol{\Xi}) + e^{-it\omega_{13}}\cos^2(\boldsymbol{\Xi})$
$S_6^{(+1)}(t)$	$e^{-it\omega_{24}}\sin^2(\boldsymbol{\Xi}) + e^{-it\omega_{34}}\cos^2(\boldsymbol{\Xi})$
$S_1^{(+2)}(t)$	$e^{-it_1\omega_{14}}$

3.2. One dimensional signal: Analytical Expressions for four-, five- and six- pulse DQC signals

In this section, expressions for four-, five-, and six-pulse DQC signals at the top of the echo will be derived analytically using the procedure outlined in Sec. 3 above for the case of nonselective pulses, i.e., strong pulses, such that $H_p \gg H_0$. The free evolution part and the pulse propagator can be simplified in this limit as follows.

It is seen from the Eqs. (16)-(19) and Table 1 that the time-dependent part of a signal due to the free evolution over coherence pathways, depends on $S_m(t), S_m(t)^*, m = 1, \ldots, 6$, which contain the terms $e^{-i\omega_{ij}t_1}$ and $e^{i\omega_{ij}t_2}$, respectively, where $\omega_{ij} = (E_i - E_j)/\hbar$; the E_i, and E_j are defined by Eq. (B.10) in Appendix B below. Using the approximation for "sufficiently broad spectral excitation" [3] i.e., $|C_1 - C_2| \gg d(3\cos^2\theta - 1)$, the pseudo-secular terms (the H_{23} and H_{32} terms in Eq. (B.5) in Appendix B) become negligible and the term $\left(\frac{d}{4}\left(3\cos^2\theta - 1\right)\right)^2$ appearing in Eq. (B.10) can be ignored compared to the Zeeman and hyperfine interactions. In this broad spectral excitation approximation limit, the explicit expressions for ω_{ij} are then:

$$\begin{aligned}
\hbar\omega_{12} &= k\sqrt{A_2^2 + 4B_2^2 k} + C_2 + \frac{1}{2}d(3\cos^2\theta - 1),\\
\hbar\omega_{13} &= k\sqrt{A_1^2 + 4B_1^2 k} + C_1 + \frac{1}{2}d(3\cos^2\theta - 1),\\
\hbar\omega_{24} &= k\sqrt{A_1^2 + 4B_1^2 k} + C_1 - \frac{1}{2}d(3\cos^2\theta - 1),\\
\hbar\omega_{34} &= k\sqrt{A_2^2 + 4B_2^2 k} + C_2 - \frac{1}{2}d(3\cos^2\theta - 1).
\end{aligned} \tag{20}$$

Since $H_{23} \approx 0$, the matrix elements Ξ_i defined by Eq. (B.8), which are used in $S_i(t_k)$; $i =$

$1,\ldots,6;\ k=1,2$, given in Table 1, become negligible. The analytical expression for the pulse propagator, i.e., $e^{-iH_pt_p}$, in the magnetic basis is, as calculated using *Mathematica*:

$$e^{-iH_pt_p}=\begin{pmatrix} \cos^2(\frac{\beta}{2}) & -\frac{i}{2}e^{-i\phi}\sin(\beta) & -\frac{i}{2}e^{-i\phi}\sin(\beta) & \frac{1}{2}e^{-2i\phi}(\cos(\beta)-1) \\ -\frac{i}{2}e^{i\phi}\sin(\beta) & \cos^2(\frac{\beta}{2}) & \frac{1}{2}(\cos(\beta)-1) & -\frac{1}{2}ie^{-i\phi}\sin(\beta) \\ -\frac{i}{2}e^{i\phi}\sin(\beta) & \frac{1}{2}(\cos(\beta)-1) & \cos^2(\frac{\beta}{2}) & -\frac{1}{2}ie^{-i\phi}\sin(\beta) \\ \frac{1}{2}e^{2i\phi}(\cos(\beta)-1) & -\frac{1}{2}ie^{i\phi}\sin(\beta) & -\frac{1}{2}ie^{i\phi}\sin(\beta) & \cos^2(\frac{\beta}{2}) \end{pmatrix}, \quad (21)$$

where $\beta=\gamma_eB_1t_p$ is the tip angle.

3.2.1. Four-pulse DQC Signal

The four-pulse DQC pulse sequence is shown in Fig 2(a). In this sequence, the first pulse $(\pi/2)_x$ generates the single-quantum coherence pathway ($p=+1$), over which it evolves for a period t_1. The second $(\pi/2)_x$ pulse transfers this magnetization to $p=\pm2$ as well as $p=0$ coherence pathways and the density matrix evolves on it over the period t_2. Thereafter, the third refocussing pulse $(\pi)_x$ transfers the density matrix to the double quantum $p=\mp2$ and $p=0$ coherence pathways, over which the density matrix undergoes free evolution for the time interval t_3. The fourth $(\pi/2)_x$ pulse finally transfers the density matrix to the single quantum coherence pathway $p=-1$, on which the signal is detected after the time interval t_4. In the experiment, t_1 is stepped and $t_2=t_3=t_{DQ}^{(4)}$ is kept fixed. The echo in this four-pulse DQC sequence occurs at the time $t_4=t_1$.

There are three different coherence pathways which contribute to the four-pulse DQC signal $(i)\ p:0\to+1\ \to2\to-2\to-1;(ii)\ p:0\to+1\ \to-2\to+2\to-1;(iii)\ p:0\to+1\ \to0\to0\to-1$. The signal from the first and second coherence pathways are calculated to be the same, each being:

$$=\frac{i}{2}\cos^2\left(\frac{1}{2}\left(j\sqrt{A_1^2+4B_1^2j}-k\sqrt{A_2^2+4B_2^2k}+C_1-C_2\right)t_1\right)\sin^2\left(\frac{at_1}{2}\right). \quad (22)$$

In Eq. (22), $a=d\left(3\cos^2\theta-1\right)$. As for the signal due to the coherence pathway (iii), it is calculated to be

$$=-\frac{i}{4}(-(\cos(at_1)-1)\times\cos((j\sqrt{A_1^2+4B_1^2j}-k\sqrt{A_2^2+4B_2^2k}+C_1-C_2)t_1)+3\cos(at_1)+1). \quad (23)$$

Finally, the total 4-pulse DQC signal is the sum of these three signals:

$$\text{Signal}_4^{DQC}(t_1)=-\,i\cos(at_1). \quad (24)$$

3.2.2. Five-pulse DQC Signal

The five-pulse DQC pulse sequence is shown in Fig. 2(b). Here, compared to four-pulse DQC sequence, an additional refocusing pulse $(\pi)_x$ is added after the last pulse. After the application of the first $(\pi/2)_x$ pulse, the system can evolve freely over time t_1 on coherence pathway $p=+1$ before the application of the second $(\pi/2)_x$ pulse, after which the coherence pathways $p=\pm2$ are chosen. After the free evolution over time t_2, the third refocussing pulse $(\pi)_x$ transfers the density matrix to the double quantum $p=\mp2$ over which the density matrix evolves for the time interval t_3. The fourth $(\pi/2)_x$ in this pulse sequence generates $p=+1$ coherence pathway over which the system undergoes a free evolution for time t_4. Finally, the fifth $(\pi/2)_x$ pulse

converts the density matrix into the observable $p = -1$ coherence pathway. The time interval between the first and the last pulse is here kept constant, to be equal to t_{max}, and t_1 is varied. The echo is detected at the time t_{max} after the last pulse, independent of the varied time t_1. For this five-pulse sequence, the constant times $t_2 = t_3$, corresponding to the pathways $p = \pm 2$, will be denoted as the double quantum time $t_{DQ}^{(5)}$.

The coherence pathways involved in the five-pulse DQC sequence are: (i) $p:\ 0 \to +1\ \to +2 \to -2 \to 1 \to -1$ and (ii) $p:\ 0 \to +1\ \to -2 \to +2 \to 1 \to -1$. Each coherence pathway contributes equally to the final five-pulse DQC signal. Finally, the total five-pulse DQC signal is:

$$\text{Signal}_5^{DQC}(t_1) = iV \sin\left[a(t_1 - \frac{1}{2}t_{max})\right], \tag{25}$$

where $V = \sin\left(\frac{1}{2}at_{max}\right)$.

3.2.3. Six-pulse DQC Signal

The pulse sequence and the coherence pathways involved in six-pulse DQC are shown in Fig. 2 (c) [1–3]. It consists of three-pulse preparation sequence $(\pi/2)_x - t_1 - \pi_x - t_2 - (\pi/2)_x$, which generates double-quantum (DQ) coherence. It is then refocused after the time t_3 by the $\pi_x - t_4$ sequence. The fifth, $(\pi/2)_x$, pulse produces anti-phase coherences, which evolve into observable single quantum coherences. Finally, the sixth, π_x, pulse, applied after the time t_5, refocuses them to form an echo. Here $t_1 (= t_2)$ is varied with fixed time $t_{max} = t_1 + t_5$, wherein, t_1 is stepped from zero to t_{max}. As well, $t_3 = t_4 = t_{DQ}^{(6)}$, which is the period for the double-quantum filter, over which the spins are on the double quantum, $p = \pm 2$, pathways, over a constant time in the experiment. $t_5 = t_{max} - t_1$ and $t_6 = t_5 + t_{echo}$. The echo in this six-pulse DQC sequence occurs at the time $t_{echo} = 0$, i.e., when $t_6 = t_5$. In the present calculations, the time variable $t_{dip} = t_{max} - 2t_1$ is used to calculate the final DQC signal as $S\left(t_{dip},\ \eta, \lambda_1, \lambda_2\right)$.

The four coherence pathways involved in six-pulse DQC as shown in Fig 2(c) are: (i) $p:\ 0 \to +1\ \to -1 \to +2 \to -2 \to 1 \to -1; (ii)$ $p:\ 0 \to +1\ \to -1 \to -2 \to +2 \to 1 \to -1; (iii)$ $p: 0 \to -1\ \to +1 \to +2 \to -2 \to 1 \to -1; (iv)$ $p:\ 0 \to -1\ \to +1 \to -2 \to +2 \to 1 \to -1$. The analytical expression for each of these coherence pathways is calculated to be the same. Finally, the overall signal is expressed as

$$\text{Signal}_6^{DQC}\ (t_1) = i\left[K - \cos\left\{a\left(t_1 - \frac{1}{2}t_{max}\right)\right\}\right], \tag{26}$$

where $K = \cos\left(\frac{1}{2}at_{max}\right)$.

It is seen from Eq. (26) that the six-pulse DQC signal has an additive constant term determined by K, so the signal is shifted by this amount. However, the time-dependent term in the signal is $\cos\left\{a\left(t_1 - \frac{1}{2}t_{max}\right)\right\}$ that determines the Fourier transform of the signal, from which the distance between the two nitroxide dipoles of the biradical can be estimated.

An inspection of Eqs. (24)–(26) reveals that the Fourier transform of any - four-, five-, or six-pulse sequence as a function of t_1 will have peaks at $\pm\ a$, where $a = \ d\left(3\cos^2\theta - 1\right)$. Furthermore, there is no dependence of the signals, given by Eqs. (24)-(26), upon the Euler angles of the two nitroxides, so an average over the Euler angles is not needed to find Pake doublets.

It is noted that, the analytical expressions of Eqs. (24)-(26) which are found by applying the algorithm given in Sec. 2, are in agreement with the analytical expressions given in [3], derived using the product operator (PO) method [19].

3.3. Two-dimensional signal

The two-dimensional signals for four-, five- and six-pulse DQC are obtained by extending the calculations of the one-dimensional signals to include a second time variable It is carried out here by replacing the time after the last pulse, which are t_4, t_5 and t_6 in four-, five- and six-pulse DQC sequences, respectively, by

$$\begin{aligned} t_4 &\to t_1 + t_{echo}^{(4)} \qquad \text{for four-pulse DQC,} \\ t_5 &\to t_{max} + t_{echo}^{(5)} \qquad \text{for five-pulse DQC,} \\ t_6 &\to t_5 + t_{echo}^{(6)} \qquad \text{for six-pulse DQC,} \end{aligned} \tag{27}$$

where $t_{echo}^{(4)}, t_{echo}^{(5)}$ and $t_{echo}^{(6)}$ are the second time variables which are stepped from the top of the echo in four-, five- and six- pulse DQC sequences, respectively. Using the algorithm given in Sec. 3.1, the two-dimensional signals for four-, five- and six-pulse DQC signals are found to be

$$\begin{aligned} \text{Signal}_4^{DQC}\left(t_1, t_{echo}^{(4)}\right) &= \text{Signal}_4^{DQC}\left(t_1\right) \times G\left(t_{echo}^{(4)}\right), \\ \text{Signal}_5^{DQC}\left(t_1, t_{echo}^{(5)}\right) &= \text{Signal}_5^{DQC}\left(t_1\right) \times G\left(t_{echo}^{(5)}\right), \\ \text{Signal}_6^{DQC}\left(t_1, t_{echo}^{(6)}\right) &= \text{Signal}_6^{DQC}\left(t_1\right) \times G\left(t_{echo}^{(6)}\right), \end{aligned} \tag{28}$$

where

$$\begin{aligned} G\left(t_{echo}^{(i)}\right) = \frac{1}{3} e^{\frac{1}{2} i a t_{echo}^{(i)}} \Big[& e^{-i t_{echo}^{(i)} (\sqrt{A_1^2 - 4B_1^2} - C_1)} + e^{i t_{echo}^{(i)} (\sqrt{A_1^2 + 4B_1^2} + C_1)} + e^{-i t_{echo}^{(i)} (\sqrt{A_2^2 - 4B_2^2} - C_2)} \\ & + e^{i t_{echo}^{(i)} (\sqrt{A_2^2 + 4B_2^2} + C_2)} + e^{i C_1 t_{echo}^{(i)}} + e^{i C_2 t_{echo}^{(i)}} \Big]. \end{aligned} \tag{29}$$

In Eq. (29), $i = 4, 5, 6$ for four-, five- and six-pulse DQC signal, respectively. The Fourier transform of the two-dimensional signal with respect to $t_{echo}^{(i)}$ gives the ESR signal in the frequency domain of the biradical, keeping the static field fixed at B_0. The coefficients $A_i, B_i, C_i, i = 1, 2$ in Eq. (29) can be calculated using Eqs. $(A.4) - (A.6)$ of Appendix A. However, Fig. 6 does not include the signal in the frequency domain calculated on the basis of these analytical expressions, since it is more convenient to calculate it using numerical algorithm, which is more exact at the same time.

It is noted that Eqs. (22)-(29) are only valid when $d(3\cos^2\theta - 1) \ll |C_1 - C_2|$ as mentioned earlier in Sec. 3.2. This is known as pseudosecular approximation. When this condition is not satisfied, one needs to carry out the simulation of the spectrum rigorously using the numerical procedure included in this paper, taking into account both the secular and the pseudosecular terms of the spin Hamiltonian.

4. Rigorous numerical simulation of multi-pulse EPR Signals in the absence of relaxation

Multi-pulse analytical expressions are rather long and unwieldy, susceptible to human error in transcribing them to calculate numerical values, although they are useful in deducing important features of the signal and its Fourier transform, as discussed in Sec, 3 above. The most efficient and rigorous method of calculating multi-pulse EPR signals is by using numerical algorithms, using the eigenvalues and eigenvectors of the Hamiltonian matrix.

To calculate the n-pulse ($n = 4, 5, 6$) signal in the absence of relaxation, one can do the calculations entirely in Hilbert space. One starts with the initial density matrix in the direct-product space as given by Eq. (15). The final density matrix $\rho_f(\mathbf{t}_k)$ with $\mathbf{t}_k = (t_1, \ldots, t_n)$ is

obtained by successive applications of the n pulses to it using Eq. (7), followed by free evolutions over the coherence pathways as shown in Fig. 2 for each pulse sequence using Eqs. (11) and (12) in the absence of relaxation. The complex signal is then obtained by using Eq. (13). The proper Gaussian inhomogeneous broadening factor is then multiplied by the calculated signal as described in Sec. 2 above.

For a polycrystalline sample, the multi n-pulse signal is calculated by (i) taking the average over a unit sphere of the signal, $S(\{\mathbf{t}_k\},\eta,\lambda_1,\lambda_2)\,;k=1,...,n$, for chosen orientations of the dipolar axis of the two nitroxide dipoles with respect to the dipolar axis, oriented at an angle θ with respect to the laboratory axis for (θ,ϕ), as well as averaging over the five independent Euler angles $(\beta_1,\gamma_1,\alpha_2,\beta_2,\gamma_2)$, keeping the Euler angle $\alpha_1=0$, which is arbitrary. Hereafter, the set of angles $(\theta,\ \phi)$, defining the orientation of the external magnetic field with respect to the dipolar axis and $(\alpha_1=0,\beta_1,\gamma_1);(\alpha_2,\beta_2,\gamma_2)$ will be, respectively, denoted as η and $\lambda_j;j=1,2$. The time-domain signal is then obtained by averaging the signals, $S(\{\mathbf{t}_k\},\eta,\lambda_1,\lambda_2)\,;k=1,...,n$, for an n-pulse sequence, over a quarter of the unit sphere (due to symmetry) over (θ,ϕ), followed by Monte Carlo averaging over random sets of the Euler angles λ_1,λ_2, as

$$S(\{\mathbf{t}\}_k)=4\sum_{\lambda_1,\lambda_2}\int_0^{\pi}d\phi\int_0^{\pi/2}S(\{\mathbf{t}_k\},\eta,\lambda_1,\lambda_2\ )\,d(\cos\theta);\quad k=1,2,\ldots,n. \tag{30}$$

As for averaging over the ensemble of five Euler angles, it is carried out here by Monte Carlo simulations, wherein the five Euler angles varied are chosen by the use of random numbers. A set of twenty such simulations seems to be sufficient as our simulations shows. Thus, a total of 90θ-values and 90ϕ-values were used over a unit sphere, along with 20 sets of five Euler angles (λ_1,λ_2). This amounts to an average over $90\times90\times20=1.62\times10^5$ simulations. The procedure to calculate the six-pulse DQC signal is outlined in a flowchart in Appendix **??**.

5. Relaxation

The effect of the relaxation on the signal is considered in this section. Section 5.1 discusses the effect of relaxation for a chosen set of the angles η,λ_1,λ_2 describing the orientations of the dipolar axis and the two nitroxide dipoles of the biradical. These expressions are then exploited to calculate the signal for a polycrystalline sample, as affected by relaxation.

5.1. Relaxation for chosen orientations $(\eta,\lambda_1,\lambda_2)$

According to Eqs. (11) and (12), the effect of the relaxation for a single-orientation of the external magnetic field with respect to the crystal axes after time t is described by multiplying the calculated signal by an exponential factor $\exp\left(-t/T_2^S\right),\exp\left(-t/T_2^D\right)$ and $\exp\left(-t/T_1\right)$ for coherence pathways $p=\pm1,p=\pm2$ and $p=0$, respectively, with the time constants T_2^S,T_2^D,T_1 appropriate for that orientation. Then the cumulative effect of the relaxation on the multi-pulse signals, considering all coherence pathways as shown in Fig. 2, is tantamount to a multiplication of four, five and six decaying exponential functions for four-pulse, five-pulse and six-pulse arrangements, respectively, with the relevant time constants multiplied by the calculated signal for the single orientation of the magnetic field with respect to the crystal axes as calculated in the absence of any relaxation. For a given value of the orientations $\zeta=(\lambda_1,\lambda_2,\eta)$, the effect of

the relaxation at the top of the echo can be expressed as

$$S_4{}^{DQC}\left(\{\mathbf{t_4}\},\zeta\right) = S_0^{(A)}\left(\{\mathbf{t_4}\},\zeta\right)\exp\left(-2t_{DQ}^{(4)}/T_2^D\left(\zeta\right) - 2t_1/T_2^S\left(\zeta\right)\right)$$
$$+ S_0^{(B)}\left(\{\mathbf{t_4}\},\zeta\right)\exp\left(-2t_2/T_1\left(\zeta\right) - 2t_1/T_2^S\left(\zeta\right)\right), \quad (31)$$

$$S_5{}^{DQC}\left(\{\mathbf{t_5}\},\zeta\right) = S_0\left(\{\mathbf{t_5}\},\zeta\right)\exp\left(-2t_{DQ}^{(5)}/T_2^D\left(\zeta\right) - 2t_{max}/T_2^S\left(\zeta\right)\right), \quad (32)$$

$$S_6{}^{DQC}\left(\{\mathbf{t_6}\},\zeta\right) = S_0\left(\{\mathbf{t_6}\},\zeta\right)\exp\left(-2t_{DQ}^{(6)}/T_2^D\left(\zeta\right) - 2t_{max}/T_2^S\left(\zeta\right)\right), \quad (33)$$

where $S_0\left(\mathbf{t_i},\zeta\right); i = 4,5,6$ are the signals calculated for the orientation ζ in the absence of any relaxation. In Eq. (31), t_2 is the time of free evolution over the coherence pathway $p = 0$ after the second pulse and $S_0^{(A)}$ and $S_0^{(B)}$ are the four-pulse DQC signals calculated in the absence of the relaxation over the coherence pathway routes $(A)\ +1\ \rightarrow \pm 2 \rightarrow \pm 2 \rightarrow -1$ and $(B)\ +1\ \rightarrow 0 \rightarrow 0 \rightarrow -1$, respectively.

5.2. Relaxation in a polycrystalline sample

5.2.1. Stretched exponential approach

For a polycrystalline sample, the signal is averaged over different values of (θ,ϕ), the orientation of the dipolar axis in the laboratory frame, characterized by different relaxation times $T_1\left(\zeta\right)$, $T_2^S\left(\zeta\right)$, $T_2^D\left(\zeta\right)$ on the coherence pathways $p = 0,1,2$, respectively. In the stretched exponential approach [14,15] one considers relaxation over a polycrystalline sample by multiplying the signal for any orientation $(\eta,\lambda_1,\lambda_2)$ by the same factor, called stretched exponential, $\exp\left(-\left[t/T_{str}\right]^{\beta}\right)$, where t is the time for relaxation and T_{str} is the average relaxation time over all orientations, and β is the stretched-exponential exponent.

5.2.2. Application to 4-, 5-, and 6-pulse DQC signals

The effect of relaxation at the top of the echo, i.e., at $t_4 = t_1$ for four-pulse DQC, at $t_5 = t_{max}$ for five-pulse DQC and at $t_6 = t_5$ for six-pulse DQC, is then expressed as

$$S_4{}^{DQC}\left(\{\mathbf{t_4}\}\right)_{Avg} = \sum_{\zeta} S_4{}^{DQC}\left(\{\mathbf{t_4}\},\zeta\right), \quad (34)$$

$$S_5{}^{DQC}\left(\{\mathbf{t_5}\}\right)_{Avg} = \sum_{\zeta} S_5{}^{DQC}\left(\{\mathbf{t_5}\},\zeta\right), \quad (35)$$

$$S_6{}^{DQC}\left(\{\mathbf{t_6}\}\right)_{Avg} = \sum_{\zeta} S_6{}^{DQC}\left(\{\mathbf{t_6}\},\zeta\right), \quad (36)$$

where the subscript Avg denotes the average over the orientations $\zeta = (\eta,\lambda_1,\lambda_2)$. Assuming the same dependence on ζ of the three relaxation times $T_1\left(\zeta\right)$, $T_2^S\left(\zeta\right)$ and $T_2^D\left(\zeta\right)$, Eqs. (34)-(36), can be expressed, in the stretched exponential approach, as follows [14,15]:

$$S_4{}^{DQC}\left(\{\mathbf{t_4}\}\right)_{Avg} = S^{(A)}\left(\{\mathbf{t_4}\}\right)\ \exp\left(-\left[2t_{DQ}^{(4)}/T_{2str}^D + 2t_1/T_{2str}^S\right]^{\beta}\right)$$
$$+ S^{(B)}\left(\{\mathbf{t_4}\}\right)\ \exp\left(-\left[2t_2/T_{1str} + 2t_1/T_{2str}^S\right]^{\beta}\right), \quad (37)$$

$$S_5{}^{DQC}\left(\{\mathbf{t_5}\}\right)_{Avg} = S\left(\{\mathbf{t_5}\}\right)\exp\left(-\left[2t_{DQ}^{(5)}/T_{2str}^D + 2t_{max}/T_{2str}^S\right]^{\beta}\right), \quad (38)$$

$$S_6{}^{DQC}\left(\{\mathbf{t_6}\}\right)_{Avg} = S\left(\{\mathbf{t_6}\}\right)\exp\left(-\left[2t_{DQ}^{(6)}/T_{2str}^D + 2t_{max}/T_{2str}^S\right]^{\beta}\right), \quad (39)$$

where $S(\{\mathbf{t_i}\})$, $i = 4, 5, 6$ are the averages of the four-, five- and six-pulse DQC signals, respectively, over all the orientations ζ, as calculated by using Eq. (30). The $T_{1str}, T_{2\ str}^{S}$ and $T_{2\ str}^{D}$ are the "stretched" relaxation times over zero ($p = 0$), single ($p = 1$ pathway) and double ($p = 2$ pathway) quantum states, respectively. The stretching parameter, β, which is related to the distribution function of the relaxation times ranges between zero and one [14,15]. Equations (37) -(39) reduce to the system with orientation-independent relaxation times in the limit when $\beta \to 1$. It is noted that, in general, there are three different stretching parameters, $\beta^{(0)}, \beta^{(S)}$ and $\beta^{(D)}$, characterizing the orientational distribution of the zero, single and double quantum relaxation times, respectively, which are to be found by fitting the simulation to the experimental data [14,15]. In this paper, since the experimental values for $\beta^{(0)}\beta^{(S)}$ and $\beta^{(D)}$ are not available, they are all assumed to be the same, i.e., $\beta^{(0)} = \beta^{(S)} = \beta^{(D)} = \beta =$ 0.8, being the average of the two values 0.78 and 0.85, derived in [14, 15].

It is noted that the effect of relaxation on five- and six-pulse DQC signals can be considered by multiplying the signal calculated in the absence of relaxation by the exponential factors, given by Eqs. (38) and (39), respectively. On the other hand, for the four-pulse sequence, the DQC signal, is obtained by multiplying the signal calculated in the absence of relaxation over a pathway by the relevant exponential factor, given by Eq. (37)

6. Comparison of four-, five-, and six-pulse DQC sequences for distance measurement

In this section, four-, five- and six-pulse DQC signals are compared in terms of the effect of relaxation on the signal and the intensity of their Pake doublets.

6.1. Main peaks

As seen from the analytical expressions for four-, five- and six-pulse DQC signals given in Sec. 5 above for 1D signals i.e., at the top of the echo, the signals depend only on the factor $d\left(3\cos^2\theta - 1\right)$ and all the other interactions e.g., Zeeman and hyperfine are absent. In the Fourier transform domain, these signals exhibit peaks at $\pm d\left(3\cos^2\theta - 1\right)$ for the orientation θ of the dipolar axis with respect to the magnetic field; thereby resulting in their Pake doublets at $\pm d$. Therefore, all these three pulse arrangements can be used for distance measurement in the biological systems.

In Fig. 7, the Pake doublets for four-, five- and six-pulse DQC signals are calculated using the rigorous numerical simulation as described in Sec. 4 which confirm that the Pake doublets occur at $\pm d$. To obtain the Pake doublets, the simulations were carried out over a grid of the unit sphere with a grid of 90×90 points of $\{\cos\theta, \phi\}$ for 20 sets of five Euler angles $\{(0, \beta_1, \gamma_1), (\alpha_2, \beta_2, \gamma_2)\}$ with Monte-Carlo averaging.

6.2. Effect of Relaxation

As described in Sec. 5, the effect of the relaxation is considered by multiplying the signals with appropriate exponential factors related to their coherence pathways. It is seen from Eqs. (31)-(33) that the exponential factors due to the relaxation for five- and six-pulse DQC signals do not contain any time variable, and they just depend on the constant times $t_{DQ}^{(5,6)}$ and t_{max}. Therefore, the relaxation does not affect the broadening of the Fourier transforms peaks of five- and six-pulse DQC signals and it only reduces the intensity of the peaks. However, the exponential factor in four-pulse DQC signal do contain the time variable t_1; thereby the relaxation affects the broadening as well as the intensity of four-pulse DQC Fourier transform peaks.

6.3. Intensities

For distance measurement, it is important to have an intense signal to improve S/N ratio. The analytical expressions given in Sec. 3, however, do not reveal the actual relative intensities of four-, five- and six-pulse DQC signals since nonselective pulses rather than finite pulses are used to obtain those expressions. Therefore, rigorous numerical simulations using finite pulses are carried out to compare the intensities of the Pake doublets of four-, five- and six-pulse DQC signals. From Fig. 7, the intensity of the Pake doublets obtained for four-pulse DQC signal is the largest, three times and 10 times larger than those of five- and six-pulse DQC, respectively.

The properties of four-, five- and six-pulse DQC sequences in terms of the splitting of the Pake doublet, intensity of their Fourier transform and the effect of the relaxation on them are summarized in Table 3.

7. Modulation depths of the calculated signals

The time-dependent signal at the top of the echo due to the dipolar modulation in four-, five-, and six-pulse DQC signals for a given orientation $\eta = (\theta, \phi)$ of the external magnetic field with respect to the dipolar axis connecting the two nitroxides, and the five independent Euler angles $\lambda_1 = (\alpha_1 = 0, \beta_1, \gamma_1), \lambda_2 = (\alpha_2, \beta_2, \gamma_2)$ can be expressed as [20, 21]

$$V\left(t, \eta,\ \lambda_1, \lambda_2\right) = V_0\left[1 - \lambda\left(\eta,\ \lambda_1, \lambda_2\right)\left(1 - \cos\left(\omega\left(\theta\right) t\right)\right)\right], \tag{40}$$

where V_0 is the amplitude of the signal at time $t = 0$; $\lambda\left(\eta,\ \lambda_1, \lambda_2\right)$ is the depth of the dipolar modulation at the orientation $\left(\eta,\ \lambda_1, \lambda_2\right)$ and

$$\omega\left(\theta\right) = d\left(3\cos^2\left(\theta\right) - 1\right). \tag{41}$$

The signal, as calculated using the details given in Sec. 4 for a polycrystalline sample, is then:

$$V\left(t\right) = 4\sum_{\lambda_1, \lambda_2}\int_0^{\pi} d\phi \int_0^{\pi/2} V_0\left[1 - \lambda\left(\eta,\ \lambda_1, \lambda_2\right)\left(1 - \cos\left(\omega\left(\theta\right) t\right)\right)\right]\ \sin\theta\ d\theta. \tag{42}$$

The maximum value of the resulting time-domain signal, $V_{0\ avg}$, occurs at time $t = 0$. Then it drops and oscillates around the equilibrium value, V_{eq}. As a percentage, the depth of the modulation for a polycrystalline sample, Δ is:

$$\Delta(\%) = \left(V_{0\ avg} - V_{eq}\right)/V_{0\ avg}\ \times 100. \tag{43}$$

The modulation depth, $\Delta(\%)$, for the time domain signals of four-, five- and six-pulse DQC signals, as calculated here, are listed in Table 3. It is seen that for all the three pulse sequences considered here, the dipolar depth of the dipolar modulation for each is $\Delta \approx 100\%$. These high values for the four-, five- and six-pulse DQC signals are well above 30%, realized in DEER and RIDME experiments, to be considered worthy of experimental measurements.

8. Details of simulations

In the numerical simulations for distance measurement carried out here, only one variable time is used, which is the time corresponding to the top of the echo for each pulse sequence, as described in Sec. 3. As well, the simulations for a polycrystalline sample can be carried out using a much larger grid over the unit sphere, because only one time variable is now needed. The values and definitions of the constants required in the numerical simulations, following the procedure given in Sec. 4, are listed in Table 2 below. The result obtained from the analytical

Table 2. The values of the parameters used in the simulations of the pulsed-EPR signal of the coupled nitroxide.

Parameter	Value
Static magnetic field (B_0)	6200 G
Microwave frequency	17.3 GHz
Exchange constant (J)	0 MHz
Gaussian inhomogeneous broadening parameter (Δ_G)	5 MHz
Double quantum time ($t_{DQ}^{(4)} = t_{DQ}^{(5)} = t_{DQ}^{(6)}$)	26.5 ns
Time step during the echo time	2.5 ns
Stretched exponential parameter (β)	0.8
g-matrix $\widetilde{\mathbf{g}} = (\mathbf{g_{xx}}, \mathbf{g_{yy}}, \mathbf{g_{zz}})$	(2.0086, 2.0066, 2.0032)
Hyperfine matrix $\widetilde{\mathbf{A}} = (\mathbf{A_{xx}}, \mathbf{A_{yy}}, \mathbf{A_{zz}})$	(6.0 G, 6.0 G, 35.0 G

expressions for non-selective pulses are shown for comparison. Although these results show a reasonable agreement with the experimental data, a perfect agreement of analytical simulation with the experiment is not expected, since experimental data are obtained with selective pulses, whereas the analytical expressions are obtained for non-selective pulses. On the other hand, the numerical simulations are always expected to show an excellent agreement with the experimental data, as they have not been subjected to any approximation. Of course, there are always present experimental error in the data.

8.1. Four-pulse DQC signal

The best fit to the experimental data of four-pulse DQC signal for the nitroxide biradical of the numerical simulation is shown in Fig. 3. The value of θ representing the orientation of the external magnetic field with respect to the dipolar axis of the coupled nitroxide is chosen to be 0° in accordance with the experiment. The frequency of of the microwave field used in the simulation is 17.3 GHz, in accordance with the experimental value [3]; The duration of the $(\pi)_x$ and $(\pi/2)_x$ pulses are 6.2ns and 3.6ns, respectively. The value of $t_{DQ}^{(4)} = 26.5$ns is chosen, and the step size in t_1 is 8ns, the same as those used in the experiment. The relaxation time $T_2^S = 870$ ns was found by fitting in the simulation. The value of the dipolar interaction constant used for the simulation was $d = 2.1$MHz, as reported in [3]. The simulated signal using the procedure given in Sec. 4 shows an excellent agreement with the experiment. The effect of the relaxation is seen in Fig. 3, as evidenced by the reduction of the heights of subsequent maxima, which would not happen had there not been present any relaxation effect.

8.2. Five-pulse DQC signal

The best fit to the experimental data for five-pulse DQC signal of a nitroxide biradical of the numerical simulation is shown in Fig. 4. The value of θ used for the five-pulse DQC experiment was 90° in the experiment; the same was used in the numerical simulation. All the other simulation parameters are the same as those used for the four-pulse DQC sequence. The simulated and the experimental signals are found to be in very good agreement with each other.

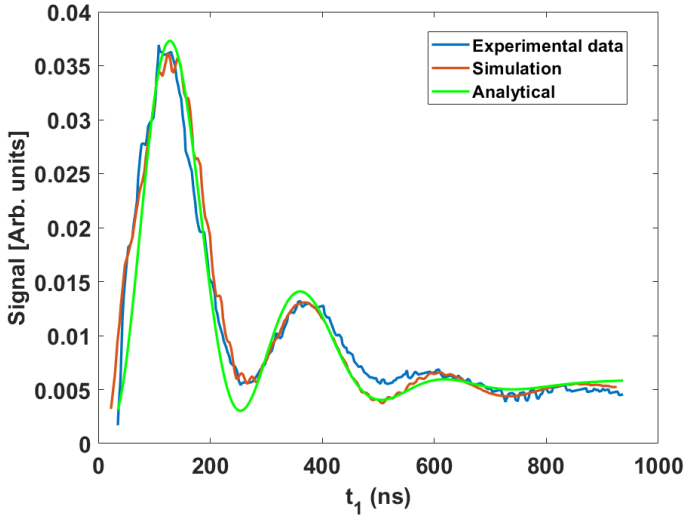

Figure 3. Experimental four-pulse DQC spectrum of the nitroxide biradical and the best least-squares fit analytical and numerical simulations, corresponding to the pulse sequence given in Fig. 1(a). The value of θ representing the orientation of the external magnetic field with respect to the dipolar axis of the couple nitroxide in the experiment is 0°. The frequency of the spectrometer used in the simulation is 17.3 GHz in accordance with the experimental value in [3]. The duration of the π and $\pi/2$ pulses are 6.2 ns and 3.6 ns, respectively. The value of $t_{DQ}^{(4)} = 26.5$ ns is chosen to be the same as that used in the experiment, and the step size in t_1 is 8 ns. This simulation carried out, using the value of the dipolar interaction constant $d = 2.1$ MHz, shows a very good agreement with the experiment, within experimental error. The experimental data is reproduced from [3].

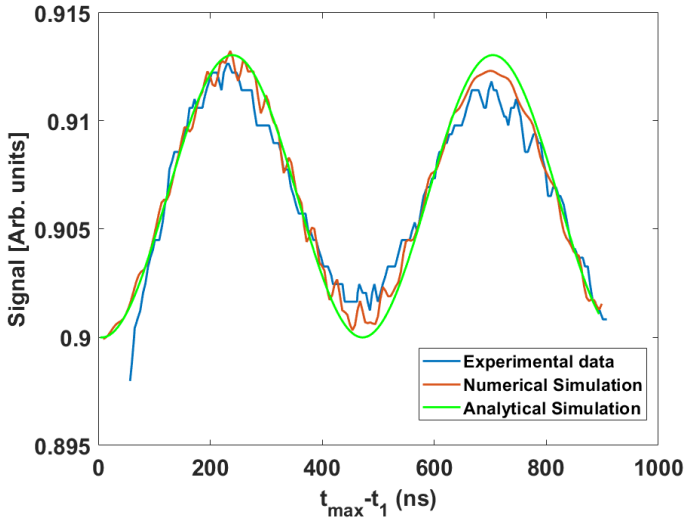

Figure 4. Experimental five-pulse DQC spectrum of the nitroxide biradical and the best least-squares fit analytical and numerical simulations. The value of θ for the five-pulse experiment was 90°. The value of the double quantum time was chosen to be $t_{DQ}^{(5)} = 26.5$ ns [3]. All the other parameters used in the simulation are the same as those mentioned in the caption of Fig. 3. The five-pulse data is plotted as a function of $t_{max} - t_1$ with $t_{max} = 947$ ns. The simulated signal calculated using the procedure given in Sec. 4 is found to be in good agreement with the experiment. The experimental spectrum is reproduced from [3].

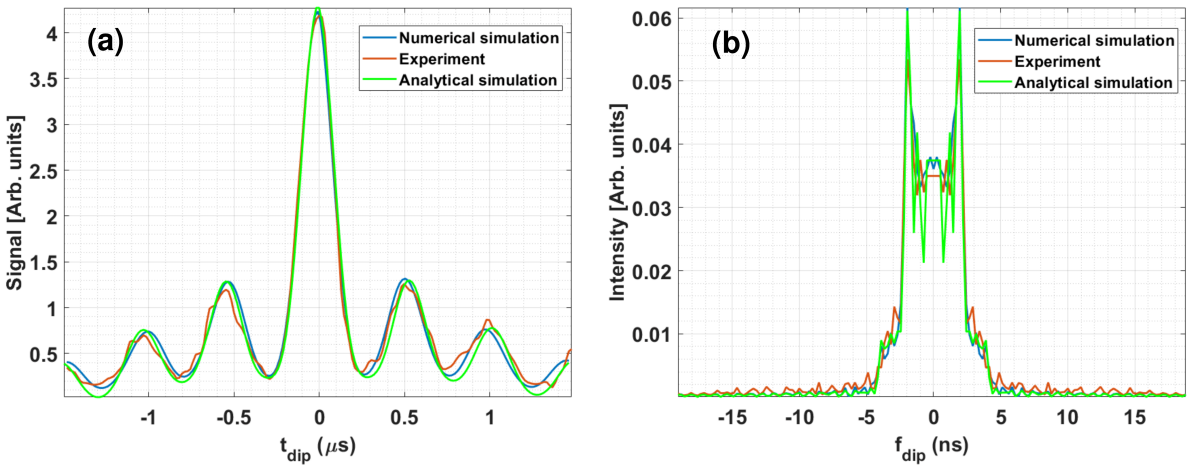

Figure 5. Experimental spectrum for a polycrystalline sample of the nitroxide biradical and the best least-squares fit analytical and numerical simulations of the six-pulse (a) DQC time domain signal and (b) its Fourier transform. The value of the double quantum time was chosen to be $t_{DQ}^{(6)} = 26.5\,\text{ns}$ [3]. All the other parameters used in the simulation are the same as those mentioned in the caption of Fig. 3. The six-pulse signal is plotted as a function of $t_{dip} = t_{max} - 2t_1$ with $t_{max} = 1200\,\text{ns}$. A baseline correction has been applied to the experimental time-domain signal. The simulation for the polycrystalline sample was carried out over a grid of the unit sphere with 90×90 points of $\{\cos\theta, \phi\}$ for 20 different sets of five Euler angles $(0, \beta_1, \gamma_1), (\alpha_2, \beta_2, \gamma_2)$ chosen by Monte-Carlo technique. The simulated signal calculated using the procedure given in Sec. 4, and its Fourier transform are in very good agreement with those of the experiment. The experimental spectra reproduced from [3].

It is noted that, since the relaxation affects equally the intensity of the five-pulse DQC signal at all time points in the plot, the two peaks shown in this figure remain with the same relative heights, as they would have been in the absence of relaxation, unlike the case of four-pulse DQC sequence.

8.3. Six-pulse DQC signal

In the present calculations of six-pulse DQC, the time variables $t_{dip} = t_{max} - 2t_1$ and $t_{echo} = t_6 - t_5$ are used to calculate the final signal as discussed in Sec. 3. The simulation of the Pake doublets was carried out over a grid of the unit sphere with 90×90 points of $\{\cos\theta, \phi\}$ with Monte-Carlo averaging over 20 sets of five Euler angles $\{(0, \beta_1, \gamma_1), (\alpha_2, \beta_2, \gamma_2)\}$. For six-pulse DQC, there are shown two figures, as follows.

(i) Figure 5 displays the experimental six-pulse DQC spectrum for a polycrystalline sample of the nitroxide biradical and the best fit numerical simulation for (a) one-dimensional time-domain signal and (b) its Fourier transform (Pake doublets). The value of the double quantum time was chosen to be $t_{DQ}^{(6)} = 26.5\,\text{ns}$, the same as that used in the experiment [3]. All the other parameters used in the simulation are the same as those listed in Table 2. The simulated six-pulse time-domain signal is plotted as a function of $t_{dip} = t_{max} - 2t_1$ with $t_{max} = 1200\,\text{ns}$ [3] in Fig. 5. The simulated time-domain signal is calculated by using the procedure given in Sec. 4. The signal and its Fourier transform are in very good agreement with those of the experiment [3].

(ii) The experimental six-pulse DQC ESR spectrum of the nitroxide biradical and the best fit numerical simulation is shown in Fig. 6. The calculated ESR spectrum, in the frequency

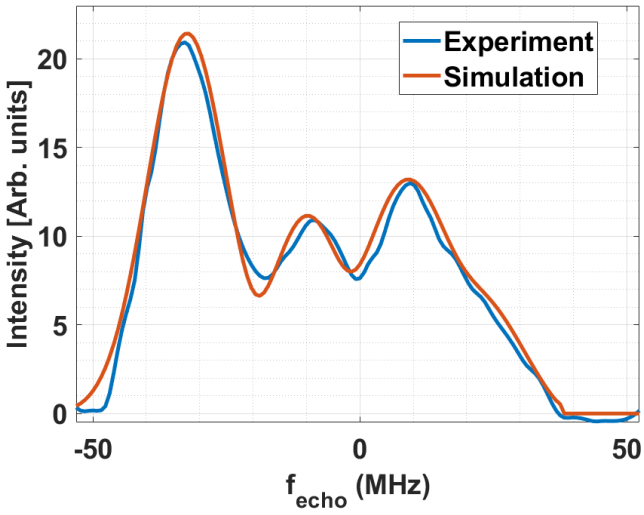

Figure 6. Experimental six-pulse DQC ESR spectrum of the nitroxide biradical and the best fit numerical simulation. The ESR frequency is a constant slice along f_{echo} of $2D$ magnitude Fourier transform vs. f_{dip} and f_{echo}, which are respective Fourier variables of t_{dip} and t_{echo}, at $f_{dip} = 2.1\,\text{MHz}$. For the simulation, the value of $(\theta, \phi) = (\pi/2, 0)$ with the combination of three sets of Euler angles which are (i) $(\alpha_1, \beta_1, \gamma_1) = (\alpha_2, \beta_2, \gamma_2) = (0, \pi/2, 0)$; (ii) $(\alpha_1, \beta_1, \gamma_1) = (0, \pi/2, 0)$, $(\alpha_2, \beta_2, \gamma_2) = (0, 0, 0)$ and (iii) $(\alpha_1, \beta_1, \gamma_1) = (0, \pi/2, 0)$, $(\alpha_2, \beta_2, \gamma_2) = (\pi/3, \pi/4, \pi/3)$ was used. The value of the double quantum time was chosen to be $t_{DQ}^{(6)} = 26.5\,\text{ns}$ [3]. All the other parameters used in the simulation are the same as those mentioned in the caption of Fig. 3. The simulated Fourier transform calculated using the procedure given in Sec. 4 is found to be in good agreement with the experiment. The experimental data is reproduced from [3].

domain, is plotted by taking a constant slice along f_{echo} of 2D Fourier transform as a function of f_{dip} and f_{echo} at $f_{dip} = 2.1\,\text{MHz}$. For the simulation, the value of $(\theta, \phi) = (\pi/2, 0)$ with the combination of three sets of Euler angles, which are (i)$(\alpha_1, \beta_1, \gamma_1) = (\alpha_2, \beta_2, \gamma_2) = (0, \pi/2, 0$;(ii) $(\alpha_1, \beta_1, \gamma_1) = (0, \pi/2, 0)$, $(\alpha_2, \beta_2, \gamma_2) = (0, 0, 0)$ and (iii) $(\alpha_1, \beta_1, \gamma_1) = (0, \pi/2, 0)$, $(\alpha_2, \beta_2, \gamma_2) = (\pi/3, \pi/4, \pi/3)$ was used. The value of the double quantum time was chosen to be $t_{DQ}^{(6)} = 26.5\,\text{ns}$ [3]. All the other parameters used in the simulation are listed in Table 2. The simulated Fourier transform calculated using the procedure given in Sec. 4 is found to be in good agreement with the experiment. This, in turn, reveals the structural detail that only certain nitroxide biradicals, characterized by a particular set of the orientations of the two magnetic dipoles of the biradical in this sample, are excited by the microwave pulse.

8.4. Comparison of the intensities of the Pake doublets in four-, five- and six-pulse DQC signals

For comparison, the intensities of the Pake doublets for 1D signals i.e., at the top of the echo, calculated for (a) four-pulse; (b) five-pulse DQ and (c) six-pulse DQC sequences are shown in Fig 7. In all these simulations, the same parameters as those listed in Table 2, along with the amplitude of the irradiation microwave field $B_1 = 60.0G$, the dipolar coupling constant $d = 10\text{MHz}$, and $t_{max} = 400\text{ns}$, are used. In order to make a realistic comparison of the various intensities, the relaxation effect is also included in all the simulations using $T_2^S = 500\text{ns}$, $T_2^D = 300\text{ns}$ and $\beta = 0.8$. It is seen that the Pake doublets occur at $\pm d$ for all the sequences. The six-pulse DQC shows the cleanest Pake pattern, whereas the Fourier transform of four-pulse

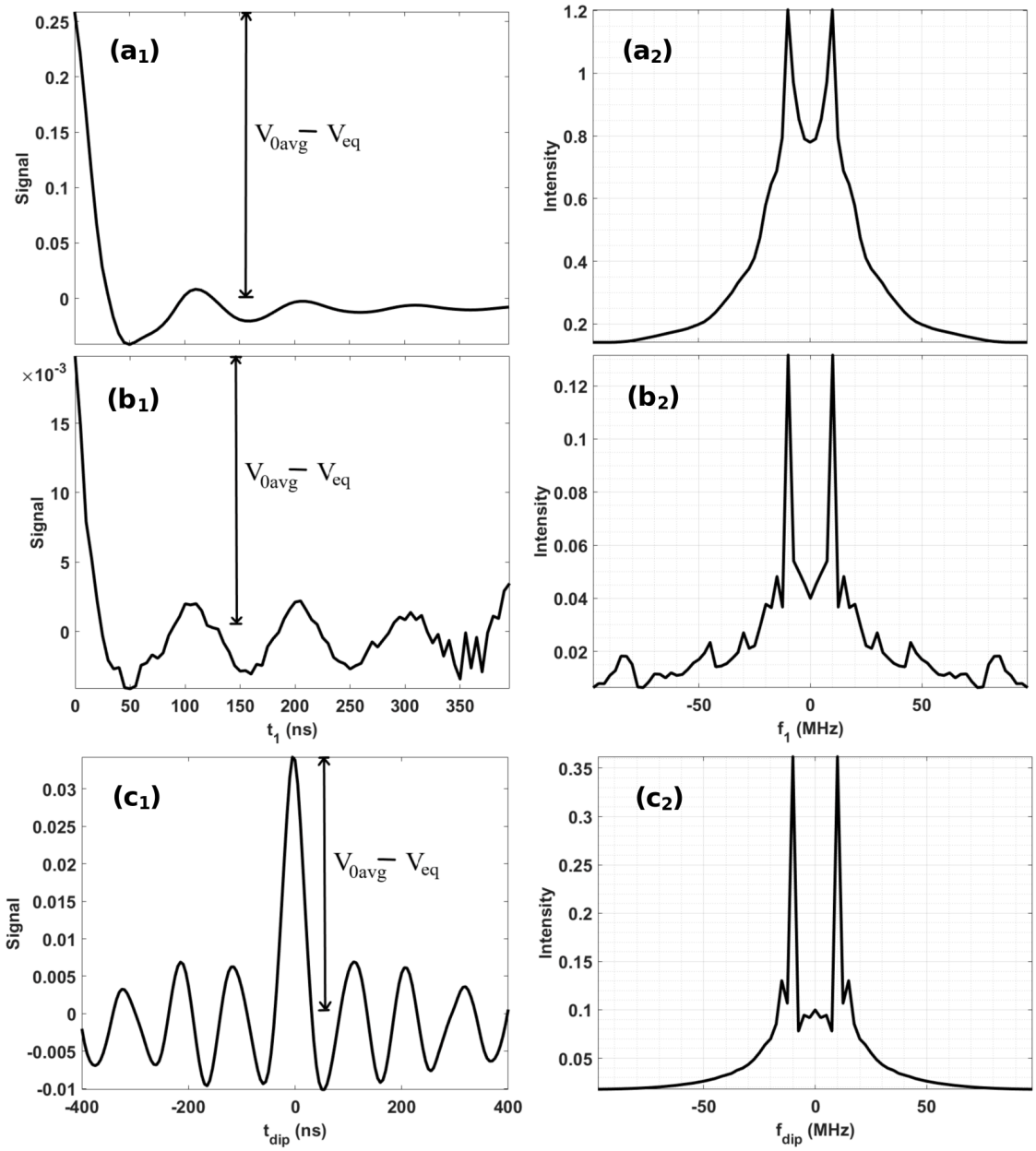

Figure 7. Comparison between the intensity of the Pake doublets obtained for (a) four-pulse; (b) five-pulse and (c) six-pulse DQC. The amplitude of the irradiation microwave field $B_1 = 60.0\,\mathrm{G}$ and the dipolar coupling constant $d = 10\,\mathrm{MHz}$ are used in the simulations. All the other parameters used are the same as those listed in Table 2. To obtain the Pake doublets, the simulations were carried out over a grid of the unit sphere with 90×90 of $\{\cos\theta, \phi\}$ points, repeated for 20 sets of Euler angles (0, β_1, γ_1),(α_2,β_2,γ_2) for a Monte-Carlo averaging. The intensity of the Pake doublet in four-pulse DQC is almost 4 times and 10 times larger than those of five- and six-pulse DQC Pake doublets, respectively. In order to make a valid comparison between the intensities, the relaxation effect is considered in all the simulations using $T_2^S = 500\,\mathrm{ns}$ and $T_2^D = 300\,\mathrm{ns}$. The depths of dipolar modulation of 100% are found in all three cases. It is noted from Figs. (a_2, b_2, c_2) that even though the Pake doublets of the four-pulse DQC sequence are broadened by relaxation, they are still sufficiently distinguishable form each other to be exploited for distance measurements. The advantage for the four-pulse DQC sequence is that the intensity of the Fourier transform is significantly larger than those of the five- and six-pulse DQC signals, although the latter have much sharper Pake doublets.

Table 3. Comparison between different pulse sequences in terms of the intensities of their Fourier transforms and the effect of the relaxation on them. The same parameters as those given in Table 1. were used in all the simulations.

Pulse sequence	Spliting of the Pake doublet	Intensity of the Pake doublet	Affected by Relaxation	Depth of the dipolar modulation
Four-pulse DQC	$\pm d$	1.2	Yes	100%
Five-pulse DQC	$\pm d$	0.13	No	100%
Six-pulse DQC	$\pm d$	0.34	No	100%

DQC is the largest in amplitude. In the simulations, the peaks of the Pake doublets are very clean in both the five- and six-pulse sequences. The resulting intensity of the Pake doublet of the four-pulse DQC simulation is four times and ten times larger than those of the five- and six-pulse DQC sequences, respectively, as seen from Table 3, listing the various intensities of the Pake doublets. It is noted that, although relaxation does not broaden the Fourier transforms of the five- and six-pulse DQC signals, their intensities are indeed reduced by relaxation.

9. Conclusions

The algorithms to calculate the signals both analytically and numerically for four-, five-, and six-pulse DQC sequences are presented in this paper. The numerical algorithm is capable of considering both selective (weak) and non-selective (strong) pulses, whereas the analytical expressions apply only to the case of non-selective pulses. The numerical simulations presented here reproduce well the published experimental data, which are obtained for selective pulses.

The salient features of the present work are as follows:

- It is shown that for the four, five- and six-pulse DQC signals the predominant peaks occur at $\pm d\left(3\cos^2\theta - 1\right)$ for the orientation of the dipolar axis of the biradical at angle (θ, ϕ) with respect to the laboratory axis (magnetic field), valid for any choices of the Euler angles, representing the orientations of the two magnetic dipoles of the biradical. This results in the maxima of their Fourier transforms in the polycrystalline averages at $\pm d$, which are also the Pake doublets in this case due to being independent of the orientations of the two nitroxide dipoles, and can be exploited for distance measurments.

- The advantage of analytical expressions, although not perfectly rigorous, is that using them one can deduce that the Fourier transforms of the signal for the three pulse sequences do not depend upon the orientations, i.e., the Euler angles characterizing them. This fact could not be seen from the numerical simulations, although they are completely rigorous.

Furthermore, the advantage of analytical expressions is that they help calculate the signal in a very short time, as compared to that required for rigorous numerical simulations. The same applies to fitting the data to evaluate the parameters, e.g. by least-squares fitting, wherein one needs to calculate the first second derivatives of the signal with respect to the fitting parameters.

- It is only the four-pulse DQC signal that depends on T_1 of the three pulse sequences considered here. Therefore, itcan be used to determine the value of T_1, knowing the value of T_2^S, e.g., from a two-pulse COSY experiment, since it depends upon both T_2^S and T_1 times.

- The simulation to fit the published experimental six-pulse DQC data on nitroxides biradicals in R-I disordered C phase-V sample [3] presented here shows that there exists correlation between the orientation of the dipolar axis with respect to the magnetic field, θ, and the orientations of the two nitroxides magnetic dipoles of the biradical, $(\alpha_1, \beta_1, \gamma_1)\,; (\alpha_2, \beta_2, \gamma_2)$. This, in turn, reveals the structural detail that only certain nitroxide biradicals, characterized by a particular set of the orientations of the two magnetic dipoles of the biradical in this sample, are excited by the microwave pulse.

- As for the relative merits of four-, five, and six-pulse DQC signals for distance measurements, it is found that (a) the widths of the Fourier transforms of the five- and six-pulse DQC signals are not affected by relaxation, whereas the width of the Fourier transform of the four-pulse DQC signal is affected significantly by both T_2^S, the single-quantum relaxation time and T_1,the spin-lattice relaxation time; and (b) the intensity of the four-pulse DQC signal is much larger, by one and two orders of magnitude, than those of six-pulse and five–pulse DQC signals, respectively.

- It is shown here that for the purpose of distance measurements one needs to consider only one-dimensional time measurements, i.e. at the top of the echo. This results in a considerable saving of computational time

Acknowledgments

We are grateful to the Natural Sciences and Engineering Council of Canada for partial financial support.

Appendices

A. Spin Hamiltonian for nitroxide biradical

The coefficients C, A and B of the spin Hamiltonian of a nitroxide are defined in this appendix. The static Hamiltonian for the coupled- nitroxide system, used in Eq. (2), can be expressed in terms of the irreducible spherical tensor operators (ISTO) as [1, 2]

$$H_{0k} = \sum_{\mu_k, L, M} F_{\mu_k, l}^{L, M^*} A_{\mu_k, l}^{L, M}, \quad k = 1, 2, \tag{A.1}$$

where μ_k indicate thes type of the interaction: g_k or A_k for Zeeman and Hyperfine interactions, respectively, $k(= 1, 2)$ specifies the two nitroxides, L is the rank of the tensor, and M takes

integer values between $-L$ and $+L$. Here l denotes the *laboratory* frame, wherein the z-axis is parallel to the static magnetic field [1]. $F^{L,M^*}_{\mu_k,l}$ are the standard ISTO components of the magnetic tensors of μ_k kind in the laboratory reference frame in Eq. (A.1), which are defined first in the magnetic g-frame of a nitroxide ($F^{L,M^*}_{\mu_k,\,g}$) and then transformed to the laboratory frame by successive transformations from the g-frame to the dipolar frame defined by its z-axis along the vector connecting the magnetic dipoles of the two nitroxides followed by the transformation to the laboratory frame. In [22] the various components of $A^{L,M}_{\mu_k,l}$ and $F^{L,M}_{\mu_k,\,g}$ are listed. In the high-field limit considered here, referred to hereafter as secular approximation, the contributions of the non-secular terms of $A^{L,M}_{\mu_k,l}$, i.e., $S_\pm, S_\pm I_z, S_\pm I_\pm, S_\pm I_\mp$, are negligible. The transformed $F^{L,M^*}_{\mu_k,l}$ can now be expressed, using the Wigner D-matrices $D^L_{m,m'}$, as

$$F^{L,M^*}_{\mu_k,l} = \sum_{m',m''} D^L_{m,m'}(\eta)\, D^L_{m',m''}(\lambda_k)\, F^{L,m''}_{\mu_k,g}, \tag{A.2}$$

where $\eta = (0,\theta,\varphi)$ and $\lambda_k = (\alpha_k,\beta_k,\gamma_k)\,; k = 1,2$ are the Euler angles defining the transformations from the laboratory frame to the dipolar frame and from the dipolar frame to the g_k frame, respectively. Inserting Eq. (A.2) into Eq. (A.1), the static Hamiltonian of two coupled nitroxides in the rotating frame in the secular approximation, i.e., neglecting the non-secular terms, is

$$H_0 = \sum_{k=1,2} H_{0k} = \sum_{k=1,2} S_{zk}\,[C_k + A_k I_{zk} + B_k I_{+k} + B_k{}^* I_{-k}], \tag{A.3}$$

where, in the rotating frame, the coefficients C_k, A_k, B_k are defined as

$$C_k = \sqrt{\frac{2}{3}} \sum_{m'} D^2_{0,m'}(\eta_k)\, K_{g_k,m'}(\lambda_k), \tag{A.4}$$

$$A_k = \sqrt{\frac{2}{3}} \sum_{m'} D^2_{0,m'}(\eta_k)\, K_{A_k,m'}(\lambda_k) + \frac{g_e\beta_e}{3\hbar}(A_{xx} + A_{yy} + A_{zz}), \tag{A.5}$$

$$B_k = \sum_{m'} D^2_{1,m'}(\eta_k)\, K_{A_k,m'}(\lambda_k). \tag{A.6}$$

The isotropic part of the Zeeman term is here put equal to zero in the rotating frame and the Zeeman term, as given by Eq. (A.4), is the "resonant offset" term, that has been quantitively calculated here. The $K_{\mu_i,m'}$ terms in Eqs. (A.4)-(A.6) which express the transformation from the magnetic frame to the dipolar frame, are defined as

$$K_{\mu_i,m'}(\lambda_i) = \left[D^2_{m',2}(\lambda_i) + D^2_{m',-2}(\lambda_i)\right] F^{2,2}_{\mu_i,g} + D^2_{m',0}(\lambda_i) F^{2,0}_{\mu_i,g}. \tag{A.7}$$

B. Matrix Representation, eigenvalues and eigenvectors of the static Hamiltonian

The magnetic basis, defined in the direct product of the electron spin basis eigenvectors $M_S = |+\rangle$ and the nuclear spin basis eigenvectors, $m_I = |-1\rangle, |0\rangle$ and $|1\rangle$, are used here for matrix representation of the static Hamiltonian. The matrix for Eq. (A.3), for example, for one of the

nitroxide biradicals, can be expressed in this basis as

$$H_{01}=\begin{pmatrix} \frac{1}{2}\left(A_1+C_1\right) & \frac{B_1}{\sqrt{2}} & 0 & 0 & 0 & 0 \\ \frac{B_1}{\sqrt{2}} & \frac{C_1}{2} & \frac{B_1}{\sqrt{2}} & 0 & 0 & 0 \\ 0 & \frac{B_1}{\sqrt{2}} & \frac{1}{2}\left(C_1-A_1\right) & 0 & 0 & 0 \\ 0 & 0 & 0 & \frac{-1}{2}\left(A_1+C_1\right) & -\frac{B_1}{\sqrt{2}} & 0 \\ 0 & 0 & 0 & -\frac{B_1}{\sqrt{2}} & -\frac{C_1}{2} & -\frac{B_1}{\sqrt{2}} \\ 0 & 0 & 0 & 0 & -\frac{B_1}{\sqrt{2}} & \frac{1}{2}\left(A_1-C_1\right) \end{pmatrix}. \tag{B.1}$$

The matrx in Eq. (B.1) is diagonalized by a unitary transformation as $E_1={T^{(1)}}^{\dagger}H_{01}T^{(1)}$, where $T^{(1)}$ is

$$T^{(1)}=\begin{pmatrix} T_{\alpha}^{(1)} & 0 \\ 0 & T_{\alpha}^{(1)} \end{pmatrix}, \tag{B.2}$$

where $T_{\alpha}^{(1)}$ is a 3×3 matrix, using the basis vectors $\left(|\psi_{-1}^{(1)}\rangle,|\psi_{0}^{(1)}\rangle,|\psi_{1}^{(1)}\rangle\right)$, as follows:

$$T_{\alpha}^{(1)}=\begin{pmatrix} \frac{A_1(A_1+\omega)+2|B_1|^2}{\omega_+} & -\frac{|B_1|}{\sqrt{2}\omega} & \frac{-A_1\omega+A_1^2+2|B_1|^2}{\omega_-} \\ \frac{\sqrt{2}(A_1+\omega)|B_1|}{\omega_+} & \frac{A_1}{\omega} & \frac{\sqrt{2}(A_1-\omega)|B_1|}{\omega_-} \\ \frac{2|B_1|^2}{\omega_+} & \frac{|B_1|}{\sqrt{2}\omega} & \frac{2|B_1|^2}{\omega_-} \end{pmatrix}, \tag{B.3}$$

where

$$\begin{aligned} \omega &= \sqrt{A_1^2+4\left|B_1\right|^2}, \\ \omega_+ &= \sqrt{2\left(A_1+\omega\right)\left(3A_1+\omega\right)\left|B_1\right|^2+A_1^2\left(A_1+\omega\right)^2+8\left|B_1\right|^4}, \\ \omega_- &= \sqrt{2\left(\omega-A_1\right)\left(\omega-3A_1\right)\left|B_1\right|^2+A_1^2\left(\omega-A_1\right)^2+8\left|B_1\right|^4}. \end{aligned} \tag{B.3a}$$

Similar results for H_{02} for the second nitroxide can be obtained by $A_1\rightarrow A_2$, $B_1\rightarrow B_2$ and $C_1\rightarrow C_2$.

For the coupled nitroxides system, the spin Hamiltonian in Eq. (A.3) has the dimension in the Hilbert space: $(2S_1+1)(2S_2+1)(2I_1+1)(2I_2+1)=36$,which can be split into sixteen 9×9 blocks, of which only six blocks have non-zero elements, as shown in the matrix of Eq. (B.5) below,. The non-zero blocks are: $(1,1),(2,2),(2,3),(3,2),(3,3)$ and $(4,4)$. Each block of this block is diagonalized by the unitary transformation $U^{\dagger}H_{ij}U$ where U is constructed from the direct product of the eigenvectors in the spin basis of the two coupled nuclei as

$$T_{\alpha}^{(1)}\otimes T_{\alpha}^{(2)}=|{\psi_j}^{(1)};{\psi_k}^{(2)}\rangle, \tag{B.4}$$

where $j,k=-1,0,1$. Using the eigenvectors of Eq. (B.4), the matrix of the static Hamiltonian of the coupled nitroxides system can be expressed as

$$H_0=\begin{pmatrix} [[H_{11}]] & [[0]] & [[0]] & [[0]] \\ [[0]] & [[H_{22}]] & [[H_{23}]] & [[0]] \\ [[0]] & [[H_{32}]] & [[H_{33}]] & [[0]] \\ [[0]] & [[0]] & [[0]] & [[H_{44}]] \end{pmatrix}. \tag{B.5}$$

In (B.5), the double square bracket [[ ]] are used to indicate a diagonal matrix in the hyperfine space. In Eq. (B.5), the blocks $H_{23}=H_{32}$, with real elements, are non-zero due to the dipolar

interaction between the two nitroxide radicals. Each matrix element in Eq. (B.5) is a 9×9 diagonal matrix, corresponding to different indices $l,\ m$ in the direct-product space, which are combinations of $j, k, j', k' = -1, 0, 1$ as follows: $l = 3j + k + 5,\ m = 3j' + k' + 5$, so that $l, m = 1, 2, \ldots, 9$. These are given by

$$
\begin{aligned}
(H_{11})_{lm} &= \{\frac{1}{2}[C_1 + C_2 + \left(A_1^2 + 4|B_1|^2 j\right)^{1/2} j + \left(A_2^2 + 4|B_2|^2 k\right)^{1/2} k] + \frac{d}{4}\left(3\cos^2\theta - 1\right)\}\delta_{lm},\\
(H_{22})_{lm} &= \{\frac{1}{2}[C_1 - C_2 + \left(A_1^2 + 4|B_1|^2 j\right)^{1/2} j - \left(A_2^2 + 4|B_2|^2 k\right)^{1/2} k] - \frac{d}{4}\left(3\cos^2\theta - 1\right)\}\delta_{lm},\\
(H_{23})_{lm} &= (H_{32})_{lm} = -\frac{d}{4}\left(3\cos^2\theta - 1\right)\delta_{lm},\\
(H_{33})_{lm} &= \{\frac{1}{2}[-C_1 + C_2 - \left(A_1^2 + 4|B_1|^2 j\right)^{1/2} j + \left(A_2^2 + 4|B_2|^2 k\right)^{1/2} k - \frac{d}{4}\left(3\cos^2\theta - 1\right)]\}\delta_{lm},\\
(H_{44})_{lm} &= \{-\frac{1}{2}[C_1 + C_2 + \left(A_1^2 + 4|B_1|^2 j\right)^{1/2} j + \left(A_2^2 + 4|B_2|^2 j\right)^{1/2} k] + \frac{d}{4}\left(3\cos^2\theta - 1\right)]\}\delta_{lm},
\end{aligned}
\tag{B.6}
$$

The static Hamiltonian H_0 in Eq. (B.5) is diagonalized by a unitary transformation $E = S^{\dagger} H_0 S$ where S is

$$
S = \begin{pmatrix} [[1]] & [[0]] & [[0]] & [[0]] \\ [[0]] & [[\xi]] & [[\zeta]] & [[0]] \\ [[0]] & [[-\zeta]] & [[\xi]] & [[0]] \\ [[0]] & [[0]] & [[0]] & [[1]] \end{pmatrix}. \tag{B.7}
$$

In Eq. (B.7), $[[\xi]]$ and $[[\zeta]]$ are 9×9 diagonal matrices in the hyperfine nuclear space, whose ith diagonal elements are $\xi_{ii} = \cos(\Xi_i)$ and $\zeta_{ii} = \sin(\Xi_i)$, respectively with

$$
\tan(2\Xi_i) = \frac{2\,(H_{23})_{ii}}{(H_{33})_{ii} - (H_{22})_{ii}}. \tag{B.8}
$$

The eigenvalue matrix of the coupled-nitroxides system is expressed as

$$
E = \begin{pmatrix} [[E_1]] & [[0]] & [[0]] & [[0]] \\ [[0]] & [[E_2]] & [[0]] & [[0]] \\ [[0]] & [[0]] & [[E_3]] & [[0]] \\ [[0]] & [[0]] & [[0]] & [[E_4]] \end{pmatrix}, \tag{B.9}
$$

where the lth ($l = 1, \ldots, 9$) diagonal elements of the various $[[E_n]], (n = 1, 2, 3, 4)$ are

$$
\begin{aligned}
&[[E_1]]_{ll} = (H_{11})_{ll},\\
&[[E_2]]_{ll} = -\frac{d}{4}\left(3\cos^2\theta - 1\right)\\
&- \sqrt{\left(\frac{d}{4}\left(3\cos^2\theta - 1\right)\right)^2 + \frac{1}{4}\left(\, C_1 - C_2 + \left(A_1^2 + 4|B_1|^2 j\right)^{1/2} j - \left(A_2^2 + 4|B_2|^2 k\right)^{1/2} k^2\right)^2},\\
&[[E_3]]_{ll} = -\frac{d}{4}\left(3\cos^2\theta - 1\right)\\
&+ \sqrt{\left(\frac{d}{4}\left(3\cos^2\theta - 1\right)\right)^2 + \frac{1}{4}\left(\, C_1 - C_2 + \left(A_1^2 + 4|B_1|^2 j\right)^{1/2} j - \left(A_2^2 + 4|B_2|^2 k\right)^{1/2} k^2\right)^2},\\
&[[E_4]]_{ll} = (H_{44})_{ll}.
\end{aligned}
\tag{B.10}
$$

In Eq. (B.10), $l = 3j + k + 5$ with $j, k = -1, 0, 1$. To calculate the density matrix during the free evolution, described by Eq. (11), one needs to calculate $e^{-iH_0 t}$, as follows transformation S as

$$e^{-iH_0 t} = S\ e^{-iEt} S^{\dagger}$$

$$= \begin{pmatrix} [[e^{-iE_1 t}]] & [[0]] & [[0]] & [[0]] \\ [[0]] & \left[\left[e^{-iE_2 t}\right]\right]\left[\left[\xi^2\right]\right] + \left[\left[e^{-iE_3 t}\right]\right]\left[\left[\zeta^2\right]\right] & [[\zeta]]\,[[\xi]]\left(\left[\left[e^{-iE_2 t}\right]\right] - \left[\left[e^{-iE_3 t}\right]\right]\right) & [[0]] \\ [[0]] & [[\zeta]]\,[[\xi]]\left(\left[\left[e^{-iE_2 t}\right]\right] - \left[\left[e^{-iE_3 t}\right]\right]\right) & \left[\left[e^{-iE_2 t}\right]\right]\left[\left[\zeta^2\right]\right] + \left[\left[e^{-iE_3 t}\right]\right]\left[\left[\xi^2\right]\right] & [[0]] \\ [[0]] & [[0]] & [[0]] & [[e^{-iE_4 t}]] \end{pmatrix}. \tag{B.11}$$

C. Projection operator matrices for the various coherence pathways

The Projection operator matrices for the various coherence pathways, which project the density matrix on to the coherence pathway of interest after the application of a pulse, are listed in this Appendix for the coherence pathways $p = \pm 1, p = \pm 2$ and $p = 0$ as used in the calculation of four-, five- and six-pulse DQC signals in Sec. 2. This is accomplished by the product $\rho^{(k)} = P_k \circ \rho$, where $P_k; k = 0, \pm 1, \pm 2$ is the projection operator matrix for the coherence pathway $p = k$ and $\circ$ denotes the Hadamard product of the two matrices, wherein each element i, j of the resulting density matrix is the product of the i, j of the projection operator matrix and the element i, j of the density matrix, ρ, the density matrix

Coherence pathway	**Matrix**
$p = +1$	$\begin{pmatrix} 0 & 1 & 1 & 0 \\ 0 & 0 & 0 & 1 \\ 0 & 0 & 0 & 1 \\ 0 & 0 & 0 & 0 \end{pmatrix}$
$p = -1$	$\begin{pmatrix} 0 & 0 & 0 & 0 \\ 1 & 0 & 0 & 0 \\ 1 & 0 & 0 & 0 \\ 0 & 1 & 1 & 0 \end{pmatrix}$
$p = 0$	$\begin{pmatrix} 1 & 0 & 0 & 0 \\ 0 & 1 & 1 & 0 \\ 0 & 1 & 1 & 0 \\ 0 & 0 & 0 & 1 \end{pmatrix}$
$p = 2$	$\begin{pmatrix} 0 & 0 & 0 & 1 \\ 0 & 0 & 0 & 0 \\ 0 & 0 & 0 & 0 \\ 0 & 0 & 0 & 0 \end{pmatrix}$
$p = -2$	$\begin{pmatrix} 0 & 0 & 0 & 0 \\ 0 & 0 & 0 & 0 \\ 0 & 0 & 0 & 0 \\ 1 & 0 & 0 & 0 \end{pmatrix}$

D. Flowchart for the calculation of the of 4-, 5-, and 6-pulse DQC signal

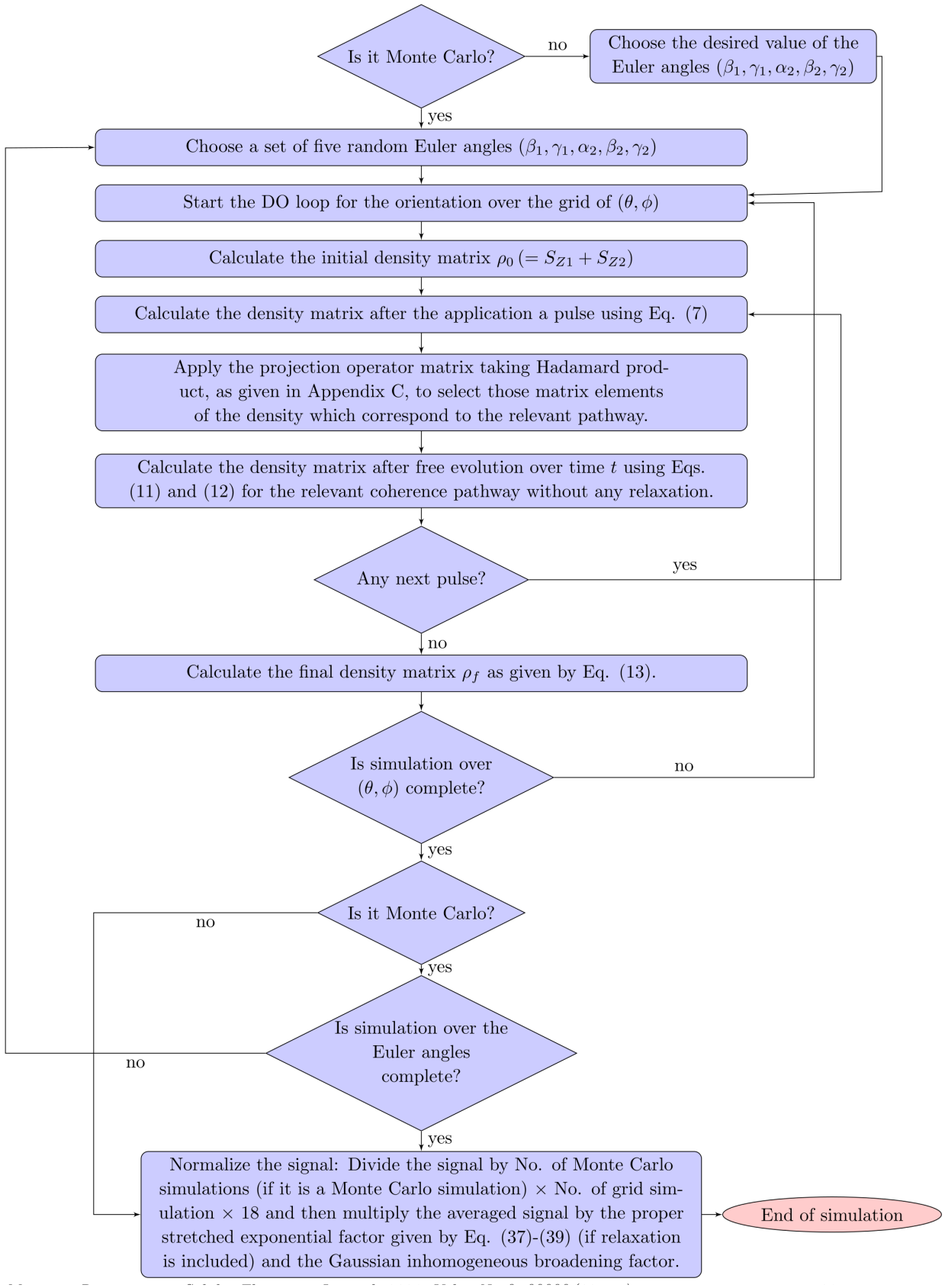

References

1. Saxena S., Freed J. H., *J. Chem. Phys.* **107**, 1317 (1997).
2. Misra S. K., Borbat P., Freed J. H., *Appl. Magn. Reson.* **36**, 237 (2009).
3. Borbat P. P., Freed J. H., *Chem. Phys. Lett.* **313**, 145 (1999).
4. Borbat P. P., Freed J. H., *EPR newsletter* **17**, 21 (2007).
5. Raitsimring A. M., Salikhov K. M., *Bull Magn Reson* **7**, 184 (1985).
6. Milov A. D., Salikhov K. M., Shirov M. D., *Sov. Phys. Solid State* **23**, 565 (1981).
7. Salikhov K. M., Dzuba S. A., Raitsimring A. M., *J. Magn. Reson.* **42**, 255 (1969).
8. Milov A. D., Salikhov K. M., Tsvetkov Y. D., *Phys. Solid State* **15**, 802 (1973).
9. Milov A. D., Tsvetkov Y. D., Formaggio F., Crisma M., Toniolo C., Raap J., *J. Am. Chem. Soc* **122**, 3843 (2000).
10. Milov A. D., Tsvetkov Y. D., Formaggio F., Crisma M., Toniolo C., Raap J., *J. Am. Chem. Soc* **123**, 3784 (2001).
11. Milov A. D., Tsvetkov Y. D., Formaggio F., Oancea S., Toniolo C., Raap J., *J. Phys. Chem. B* **107**, 13719 (2003).
12. Milov A. D., Naumov B. D., Tsvetkov Y. D., *Appl. Magn. Reson.* **26**, 587 (2004).
13. Milov A. D., Tsvetkov Y. D., *Appl. Magn. Reson* **12**, 495 (1997).
14. Stein N., Mainali L., Hyde J. S., Subczynski W. K., *Appl. Magn. Reson* **50**, 903 (2019).
15. Pfenninger S., Antholine W. E., Barr M. E., Hyde J. S., Kroneck P. M., Zumft W. G., *Biophys. J.* **69**, 2761 (1995).
16. Lee S., Patyal B. R., Freed J. H., *J. Chem. Phys.* **98**, 3665 (1993).
17. Misra S. K., Salahi H. R., *App. Magn. Reson.* **52**, 247 (2021).
18. Misra S. K., Salahi H. R., *Magn. Reson. Solids* **22**, 20101 (2020).
19. Slichter C. P., *Principles of Magnetic Resonance* (Springer Verlag, New York, 1989).
20. Jeschke G., Koch A., Jonas U., Godt A., *J. Magn. Reson.* **155**, 72 (2002).
21. Halbmair K., Wegner J., Diederichsen U., Bennati M., *Biophys. J.* **11**, 2345 (2016).
22. Berliner L. J., Ed, *Spin Labeling: Theory and Application* (Academic Press, New York, 1976).